AGU Books
Ed. Anthea Coster

Chapter: Space weather radiation effects on high altitude/latitude aircraft

Christopher J. Mertens[1] and W. Kent Tobiska[2]

[1]Senior Research Physicist, NASA Langley Research Center, Space Radiation Group, Hampton, Virginia 23681-2199 USA

[2]Chief Scientist, Space Weather Division, , Space Environment Technologies, 1676 Palisades Dr., Pacific Palisades, CA 90272 USA

Space weather radiation effects on high altitude/latitude aircraft

Abstract

The effects from ionizing radiation exposure is a concern faced by aircrew, high-altitude pilots, frequent flyers, and commercial space travelers. This chapter describes the physics of atmospheric radiation's primary sources including galactic cosmic rays (GCRs) and solar energetic particles (SEPs) as well as the possibility of a newly identified third source of secondary radiation caused by precipitating radiation belt charged particles. The primary radiation processes of transport through the heliosphere, modulation by the solar wind, and magnetic shielding by the Earth's geomagnetic field are described. The SEP primary radiation differential energy spectrum is described and radiation belt precipitated charged particles are discussed with information from a large database of atmospheric radiation measurements. The transport of charged particles from all sources through the magnetic shielding from the Earth's geomagnetic field is described and the concept of geomagnetic cutoff rigidity is thoroughly explained. The transport of radiation through the atmosphere from precipitating charged particles below the mesopause is presented from a theoretical perspective, including the interactions of neutrons and charged particles with target species in the atmosphere. Radiation dosimetry is described, including dose quantities and quality factor. Additional discussions are presented with an introduction on radiation effects on avionics, the models capable of reporting the aviation radiation environment, the measurements that have been made of the atmospheric radiation by specific instruments, and introductory remarks on the regulatory activity internationally and in the U.S. related to the effects of radiation faced by aircrew, high-altitude pilots, frequent flyers, and commercial space travelers.

Plain Language Summary

This chapter provides a thorough discussion, including the mathematical basis, explaining the source, dynamics, and characteristics of space weather driven atmospheric radiation. Fundamental concepts of radiation dosimetry, models, measurements, and regulatory activities are described.

1 Introduction

Air safety has improved significantly over the past decades with the exception of effects from space weather, which includes ionizing radiation. Radiation exposure is a natural hazard faced by aircrew, high-altitude pilots, frequent flyers, and commercial space travelers.

Multiple sources of ionizing radiation contribute dose exposure in the aerospace environment that reaches from Earth's surface into space. Galactic cosmic rays (GCRs) and solar energetic particles (SEPs) are the dominant ionizing radiation sources (Figure 1). This is especially true for travel above commercial aviation altitudes starting at 8 km (26,000 ft.) [Friedberg and Copeland, 2003, 2011; Tobiska *et al.,* 2016]. GCRs are produced outside the solar system in high-energy explosive events and mostly consist of energetic protons that penetrate the heliosphere. They are slowly modulated by the strength of the Sun's interplanetary magnetic field [Simpson, 1983]. SEPs come from solar activity such as coronal mass ejections related to flaring events or from interplanetary magnetic field shocks [Gopalswamy, 2004; Reames, 2013]. In the latter case, fast coronal mass ejections plow through both ambient background and high-speed stream solar wind fields to create a shock front that produces accelerated energetic protons. A third radiation source has been recently hypothesized, based on measurements, and likely originates from the wave-particle interaction in the Van Allen radiation belts (RB) leading to precipitated charged particles (PCPs) [Tobiska *et al.,* 2018]; substantial study is underway to understand the source of this third radiation

source of RBPCPs.

The presence of primary ionizing dose in the aerospace environment, which can be altered by the composition of the terrestrial atmosphere and the dynamic variability of the Earth's magnetosphere resulting in secondary and tertiary ionizing radiation environments, causes concern for human health and vehicle avionics. It is this motivation that directs the study of radiation environment effects on high altitude and high latitude aircraft.

2 The physics of atmospheric radiation

2.1 Galactic cosmic rays

GCRs consist of approximately 90% protons and 8% helium nuclei with the remainder being heavier nuclei and electrons [Gaisser, 1990]. After these particles penetrate the magnetic fields of the solar system and the Earth to reach the Earth's atmosphere, their collisions with air molecules create cascades of secondary and tertiary radiations [Reitz *et al.,* 1993]. The collisions are primarily due to Coulomb interactions of the GCR particle with orbital electrons of the atmospheric molecules, delivering small amounts of energy to the orbital electrons. This energy transfer process leaves behind electron-ion pairs [Wilson *et al.,* 1991]. The ejected electrons often have sufficient energy to extend ionizing events. The GCR ions lose a small fraction of their energy and endure many atomic collisions before slowing down. Occasionally the GCR ion will collide with an air molecule nucleus where large energies are exchanged, resulting in dramatic changes to the ion and nucleus. The remnant nucleus emits further air nuclear constituents by decaying through the usual radioactivity channels [Wilson *et al.,* 1991]. An important secondary particle created in the GCR-air interactions is the neutron. Because of charge neutrality, the neutron is able to penetrate deep into the atmosphere, causing further ionization events and contributing over half the atmospheric radiation exposure at typical commercial airline altitudes [Wilson *et al.,* 2003]. Furthermore, neutron exposures create a relatively high health risk since neutron interactions produce abundant ions in the cell that is impacted and repair is less efficient for these events [Wilson, 2000; Mertens *et al.,* 2012].

The intensity of the atmospheric radiations, their energy distribution, and their effects on aircraft crew and passengers vary with altitude, location in the geomagnetic field, and the Sun's magnetic activity (solar) cycle [Heinrich *et al.,* 1999; Reitz *et al.,* 1993; Wilson, 2000]. The atmosphere provides material shielding depending on the atmospheric depth overhead. The geomagnetic field provides shielding by deflection of low-momentum charged particles back into space. Because of the orientation of the dipolar geomagnetic field, the polar and high-latitude regions experience increased particle penetration. At each geographic location, the minimum momentum per unit charge, i.e., magnetic rigidity, that a vertically incident particle can have to reach a given magnetic latitude is called the vertical geomagnetic cutoff rigidity. The local incident charged particle flux varies widely with geomagnetic location and solar modulation. When solar activity is high, GCR flux arriving from outside the solar system is low and vice versa. The balance between outward convective flux of solar wind and the inward diffusive flux of GCRs is responsible for the dynamic anti-correlation between incident GCRs and solar cycle activity [Clem *et al.,* 1996; Parker, 1965].

2.2 Heliospheric GCR transport

GCRs are transported through the heliosphere to the near-Earth space environment and can be modeled using an expanded version of the Badhwar and O'Neill model [Badhwar and O'Neill, 1991; 1992; 1993; 1994; Badhwar and ONeill, 1996]. The Badhwar and O'Neill model, which is referenced as the GCR model here, was updated [O'Neill, 2006] to use ground-based neutron monitor count rates from the Climax neutron monitor site. This provided a measurement constraint on the simulated solar cycle modulation of the GCR spectrum at 1 Astronomical Unit (AU). Comparisons between the GCR model and NASA Advanced Composition Explorer (ACE) satellite CRIS instrument measurements of the GCR spectra have shown that this step has enabled accurate predictions of GCR spectra in the geospace environment on monthly to seasonal time scales [O'Neill, 2006]. O'Neill [2006] was extended by incorporating four high-latitude neutron monitor count rate measurements (Thule, Oulu, Izmiran (or Moscow), and Lomnicky) into the GCR model predictions at 1 AU [Mertens *et al.,* 2009, 2012]. These high-latitude neutron monitor locations are sensitive to the GCR spectral region most influenced by solar cycle variability and the data from these stations are available in real-time or near real-time.

Figure 2 shows the solar cycle variation in the GCR spectrum for several nuclei. The spectra were computed by the Badhwar and O'Neill model [Mertens *et al.,* 2008; 2007a]. The figure shows the LIS spectra and the spectra at solar maximum and solar minimum conditions. The solar cycle modulation of LIS as the GCR nuclei are transported through the heliosphere to 1 AU is clearly evident.

This GCR model propagates the local interstellar spectrum (LIS) of each element in the GCR composition to 1 AU by solving a steady-state, spherically symmetric Fokker-Planck transport equation containing diffusion, convection, and adiabatic deceleration of GCRs entering the heliosphere [Parker, 1965]. The transport physics enables GCR temporal and spatial dependence to be expressed as a ratio of the diffusion coefficient to the bulk solar wind speed. The ratio functional form is

$$\tilde{k}(r,t) \equiv k(r,t)/V_{SW}(r,t) = (k_0/V_{SW})\beta R\,[1 + (r/r_0)^2]/\Phi(t) \qquad (1)$$

where V_{SW} is the bulk solar wind speed set to 400 km s^{-1} for all time; r is the distance from the Sun in AU, t is time in years, k_0 and r_0 are constants, β is the particle's speed relative to the speed of light, R is the particle's magnetic rigidity in MV, and Φ is the solar modulation parameter. The GCR spectral flux time-dependent behavior due to the level of solar activity is embedded in the solar modulation parameter. The solar modulation parameter is physically related to the energy that interstellar nuclei must have in order to overcome the heliospheric potential field. The latter is established by the large-scale structure of the interplanetary magnetic field (IMF). The solar modulation parameter is determined by fitting the solution of the Fokker-Planck equation for a specified GCR nuclei to the corresponding spectral flux measurements throughout the solar cycle as described by O'Neill [2006].

Once the solar modulation parameter was derived based on satellite oxygen spectra, the LIS for the remaining elements (i.e., lithium (Z=3) through nickel (Z=28)) were similarly determined by fitting the solutions of the Fokker-Planck equation to the ACE CRIS instrument spectral flux measurements. A simple power law form of the differential LIS can be assumed,

$$j_{\mathrm{LIS}}(E) = j_0\beta^{\delta}(E + E_0)^{-\gamma} \qquad (2)$$

where E is the particle kinetic energy per nucleon and E_0 is the rest mass energy per nucleon (938 MeV/n). The free parameters (γ,δ, and j_0) were determined from the fit of the GCR model to satellite measurements.

The GCR model was extended beyond the time period of satellite measurements by first deriving the solar modulation parameter from the IMP-8 satellite channel 7 (Z >8, high energy) measurements over three solar cycles from 1973 through 2001 and then calibrating against the solar modulation parameter derived from ACE/CRIS satellite measurements for the period of data overlap (1997.6 to 2001.8). The heliospheric GCR diffusion coefficient depends on the large-scale structure of the IMF [Parker, 1965] and, thus, on the polarity of the Sun's polar magnetic field [O'Neill, 2006]. Consequently, to improve the accuracy of the neutron count rate fits to the reference Φ_{CLIMAX}, the data were sorted according to the polarity of the Sun's polar magnetic field, and three sets of fit coefficients were derived between the IMP-8 solar modulation parameter and Climax neutron monitor count rates from 1973-2001 for three polarity states of the solar polar magnetic field: (1) positive solar cycle (outward field), (2) negative solar cycle (inward field), and (3) transition state (intermediate between positive and negative polarities with a high degree of modulation) [Mertens *et al.,* 2009, 2012]. Figure 3 shows the solar polar magnetic field data since 1978, which are obtained from measurements taken at the Wilcox Solar Observatory (WSO) located at Stanford University. The solar modulation parameter was extended from 1958-2009 to provide a reference solar modulation parameter for real-time GCRs to be included in atmospheric radiation models and the solar polar magnetic field data from WSO must be added to the atmospheric radiation model input data streams.

High latitude neutron monitor sites are particularly valuable for real-time GCR models. By cross-correlating the Climax-based solar modulation parameter (Φ_{CLIMAX}) with neutron count rates measured at high-latitude sites [Mertens *et al.,* 2009, 2012], they maximize the solar cycle information content contained in the GCR spectrum via the ground-based neutron count rates. Neutrons detected on the ground are secondary particles produced by nuclear fragmentation reactions between the incoming GCR particles and atmospheric constituents [Wilson *et al.,* 1991]. At high-latitudes the geomagnetic shielding of the incoming GCR particles is low. Thus, the ground-level neutron count information is high for the low- and medium energy region of the GCR spectrum. This is desirable because this GCR spectrum energy range is most modulated by the solar wind and IMF and is closely related to solar activity cycle [Mertens *et al.,* 2008].

2.3 Solar energetic particles

Solar energetic particles (SEPs) originate from coronal mass ejections (CME) from active regions on the solar surface [Kahler, 2001; Wilson *et al.,* 2005a]. The CME propagates through interplanetary space carrying the local surface magnetic field frozen into the ejected mass along with it. There is a transition or shock region often associated between the normal background and sectored magnetic structure of interplanetary space and the fields frozen into the ejected mass. The plasma is accelerated at this shock front and forms SEPs. As an accelerated region passes an observation location, the flux intensity is observed to dramatically increase. The SEP energy spectrum obtained in the acceleration process is related to the plasma density and CME velocity. During a CME event, the number flux distribution that is incident upon Earth's atmosphere is a combination of the GCR, SEP, and RBPCP distributions. The SEP-air interaction mechanisms are the same as GCR-air interactions described above where the secondary and tertiary radiations caused vary with altitude and geomagnetic field cutoff rigidity.

Because the particles from SEP events are transported from the Sun to the near-Earth environment through the inner heliosphere, their energy spectrum results from injected particle seed populations that are stochastically accelerated in a turbulent magnetic field. That field is associated with a CME-driven interplanetary shock [Tylka and Lee, 2006]. Ellison and Ramaty [1985] provided an

analytical expression representing the differential energy spectrum for shock acceleration with the form

$$d^2J/dEd\Omega = C_a\, E^{-\gamma_a} \exp\left(-E/E_0\right) \quad (3)$$

The differential energy spectrum on the left-hand side of equation (3) has units of $(cm^2\text{-sr-hr-MeV/n})^{-1}$, and the energy (E) has units of MeV/n (i.e., MeV/nucleon). The constant value, C_a, relates to the injected seed population upstream of the shock. The power-law energy dependence of the spectrum occurs from shock acceleration of the seed population by random first-order Fermi acceleration (scattering) events in a turbulent magnetic field. The power index (γ_a) parameterizes the shock compression ratio. The exponential turnover in (3) represents high-energy limits to the acceleration mechanism with particle escape from the shock region being a prime example. Using the above analytical form, the three parameters (C_a, γ_a, and E_0) can be determined by fitting (3) to ion flux measurements.

Mewaldt *et al.* [2005] noted that the Ellison-Ramaty spectral form did not properly fit the GOES ion flux measurements in the highest energy channels during the Halloween 2003 SEP events. As a result, Mewaldt *et al.* [2005] proposed using a double power-law spectrum. The low-energy spectrum follows the Ellison-Ramaty form while the high-energy spectrum has a power-law energy dependence using a different power index, such that

$$d^2J/dEd\Omega = C_b\, E^{-\gamma_b} \quad (4)$$

The power-law expressions in (3)-(4) can be merged into one continuous spectrum by requiring that the differential energy spectra in (3)-(4) and their first derivatives are continuous at the merge energy. Mertens *et al.* [2012] show this combined form with the expression:

$$d^2J/dEd\Omega = C\, E^{-\gamma_a} \exp\left(-E/E_0\right),\ E \le (\gamma_b - \gamma_a)\, E_0 \quad (5)$$

$$= CE^{-\gamma_b} \{[(\gamma_b - \gamma_a)E_0]^{(\gamma_b - \gamma_a)} \exp(\gamma_b - \gamma_a)\},\ E > (\gamma_b - \gamma_a)E_0. \quad (6)$$

Physically, the double power-law spectrum in (5)-(6) represents SEP sources from two different injected seed populations. The low-energy spectrum, with γ_a power index and the e-folding energy E_0, is possibly associated with solar corona (solar wind) seed populations while the high-energy spectrum, with γ_b power index, is likely associated with flare suprathermal seed populations [Tylka *et al.,* 2005].

Another widely used analytical representation of a SEP energy spectrum is a Weibull distribution [Townsend *et al.,* 2003; 2006], which has been successful at fitting satellite ion flux measurements. The differential energy spectrum is given by

$$d^2J/dEd\Omega = C\, k\, \alpha\, E^{\alpha-1} \exp(-kE^{\alpha}). \quad (7)$$

The Weibull distribution has an analytical form similar to the Ellison-Ramaty distribution in (3) and the former's exponential energy dependence could be due to dissipation of high-energy SEP ions through scattering from self-generated waves. However, some researchers recommend further investigation [Xapsos *et al.,* 2000].

Models such as the NASA Langley Research Center's (LaRC) *Nowcast of Atmospheric Ionizing RAdiation System (NAIRAS)* physics-based radiation model [Mertens *et al.,* 2013] using a continuous, real-time data stream fits four analytical SEP spectral fluence rate functions to satellite ion flux measurements. The analytical forms that are fit to measurements are: (1) single power-law in (4), (2) Ellison-Ramaty in (3), (3) double power-law in (5)-(6), and (4) Weibull in (7). The free parameters for each analytical differential energy distribution are derived by a non-linear least-square fit to differential-directional ion flux measurements using a Marquardt-Levenberg iteration technique [Brandt, 1999]. NAIRAS, for example, utilizes available real-time measurements of

proton and alpha differential-directional particle flux $(cm^2\text{-sr-sec-MeV/n})^{-1}$ for the SEP spectral fitting described above. SEP spectral fluence rates (cm^2-hr-MeV/n) incident on Earth's magnetosphere are obtained by time-averaging the particle flux measurements in 1-hour time bins and projecting the incident flux onto the vertical direction assuming an isotropic angular distribution for the solar ions.

As the SEPs arrive at the top of the Earth's atmosphere, their characteristics have been pre-determined by several items. First, the geomagnetic field has a significant influence on SEP atmospheric ionizing radiation exposure. For example, the magnetospheric magnetic field can weaken the overall geomagnetic field which results in an increase in radiation levels. The cutoff rigidity values will be zero where open geomagnetic field lines exist. Thus, effective dose rates based on the solar on the Earth main field, e.g., the IGRF field, are underestimated even for magnetically quiet times. During strong geomagnetic storms, the region of open field lines is further expanded and this produces larger exposure rates at much lower latitudes. Second, there is a strong altitude dependence upon atmospheric shielding as discussed in detail later.

2.4 Radiation belt precipitated charged particles

Recent measurements [Tobiska, *et al.,* 2016; 2018; Dachev, 2017; Dachev *et al.,* 2017a] have suggested the possibility of another radiation source besides GCRs and SEPs. Liulin instrument ISS measurements [Dachev, 2017; Dachev *et al.,* 2017b] have seen radiation effects from relativistic electrons originating in the outer radiation belt (ORB). *Automated Radiation Measurements for Aerospace Safety (ARMAS)* instrument aircraft and balloon measurements have collected a large number of atmospheric observations at higher magnetic latitudes with *L* shells between 1.5 and 5. These data are gathered during quiet and minor geomagnetic disturbances including during high-speed streams. For NOAA G-scale G0 conditions at 11 km altitude near $L = 4$ the tissue-relevant effective dose rates are statistically higher than the GCR background by 15% higher (Figure 4) for many observations [Tobiska, *et al.,* 2018]. We propose that this is a new, third radiation source likely originating from charged particles that are associated with the Van Allen radiation belts. Highly variable, dynamic mesoscale radiation events at aviation altitudes are attributed to these particles as a source, where their manifestation is analogous to an aircraft flying through radiation "clouds," although physically the aircraft appears to be flying through a γ-ray beam.

A common characteristic of these enhanced radiation event periods at higher magnetic latitudes ($2 \leq L \leq 6$) is that the radiation levels during flight begin at the GCR background level, rise to almost a factor of 2 higher, and then return to background GCR levels within less than an hour. This is consistent with flight through a secondary, Bremstrahlung γ-ray beam produced by precipitating relativistic electrons that are stopped in the mesosphere, for example. Throughout the ARMAS database, there have been over 100 cases of these types of enhanced radiation events that are candidates for study related to effects from radiation belt particles [Tobiska, *et al.,* 2018].

A recent and extensive study comparing ARMAS measurements [Tobiska *et al.,* 2018] with the NAIRAS model [Mertens *et al.,* 2013] extracted GCRs and suggested relativistic electron precipitation (REP) statistics. The Tobiska *et al.* [2018] study described a subset of observations of enhanced radiation short-term events lasting tens of minutes to under two hours of dose rate enhancements occurring between 9 and 14 km altitude in a well-defined magnetic latitude band. The dose rate enhancements were not attributed to GCRs or SEPs. They explored, for example, how energetic electrons from the outer Van Allen radiation belt can be precipitated by electromagnetic ion cyclotron (EMIC) waves [Tsurutani *et al.,* 2016] associated with particle injections from geomagnetic substorms. Using modeling and observations EMIC waves were

shown as an example of how to supply a population of relativistic electrons that can subsequently become a source of radiation enhancements above the GCR background. The primaries are absorbed between 50–60 km and a fraction of their secondaries are Bremsstrahlung γ-rays that can penetrate down to 10–14 km at commercial aviation altitudes.

Lines of evidence for an energetic electron radiation source in one example were considered from many events that all have a common feature, i.e., the data in each example started near statistical and climatological GCR baseline values and from there the dose rates were observed to rise significantly above and later fall back to that baseline over tens of minutes to under two hours (Figure 5, top panel). Data in this figure were taken on aircraft from the National Science Foundation (NSF) National Center for Atmospheric Research (NCAR) Gulfstream 5 (G-5) while other ARMAS measurements were made on the National Oceanic and Atmospheric Administration (NOAA) G-4, the NASA Armstrong Flight Research Center (AFRC) DC-8 and G-3, the Federal Aviation Administration (FAA) William J. Hughes Technical Center (WJHTC) Bombardier Global 5000 (BG5) and commercial B-737, B-747, B-767, B-757, A-320, A-380, and E-175 aircraft. The criteria for selecting potential events included altitudes above 9 km, level flight during the event, magnetic latitudes corresponding to inner and outer belt L-shells (magnetic latitudes between 43° and 67° for both hemispheres, i.e., L = 1.9 to 6.8), and a significant event rise (at least 40%) above then return to GCR background values as represented by modeled results for a flight.

Figure 6 shows the ratio of ARMAS (measurement) to NAIRAS (model with only GCR contribution at this time) effective dose rates throughout each minute of many ~50^{+} magnetic latitude flights. These ratios compare ARMAS to NAIRAS for each altitude level above 8 km and for geomagnetic conditions of G0 and G1 on the NOAA G-scale. Most ratios are above 1.0 (blue) and the mean of 1537 one-minute ratio time records for all events is 1.91. In other words, there is nearly a factor of 2 increase in dose rate (green values) while flying through a radiation event compared with flying at the same altitude and under the same geomagnetic conditions under only GCR background conditions. Measurements show that there exists a defined magnetic latitude band within which these events occur and the distance L-shell [McIlwain, 1961; Tascione, 1994] range of 2–7, labeled "L2" and "L7," in the yellow as notional bands in both hemispheres are the best fit of global locations for these events. L-shells from ~3–7 are the regions where outer radiation belt charged particles map into the upper atmosphere while L-shells from ~1.3–2 are the regions where inner radiation belt charged particles map into the upper atmosphere. This L-shell band is consistent with Katsiyannis *et al.* [2018] who observed low Earth orbit relativistic electrons from the PROBA-V satellite EPT and LYRA instruments and Dachev *et al.* [2017a; b] as well as Dachev [2017] who have called these precipitation bands when observed by the Liulin instrument on the ISS.

One typical flight (Figure 5, top panel) on 03 October 2015 at 15–16 UT shows an event, circled in the figure, with an effective dose rate that rose and declined by a factor of two above GCR background levels within 33 minutes. The entire flight dataset was collected for 13.1 h between 03 October at 11:30 UT and 04 October at 00:34 UT. The event occurred for a fraction of the total flight. Uncertainties in the ARMAS data are ±24% and are described by Tobiska *et al.* [2016].

For the range of cutoff rigidities from Chile to Antarctica (Rc = 3.89 to 0.24, respectively; Figure 5) the mean radiation quality factor (Q, relevant to the dose rate in tissue) was 2.03 with a Rc dependency [Tobiska *et al.,* 2016]. The total flight effective dose was 157 μSv for the 03 October 2015 flight, i.e., the exposure of approximately one and a half chest X-rays. For this event starting at 15:07 UT (–60.1° magnetic latitude) the peak dose rate (top panel colored dots in Figure 5) occurred at 15:29 UT (11:38 Local Clock Time) when the aircraft was flying at an L-shell of 4.8 corresponding to –62.7° magnetic latitude. Background dose rates were once again reached at

15:45 UT (–64.6° magnetic latitude). The background levels were very close to the values of NAIRAS shown in the Figure 5 top panel (black "+" NAIRAS model , black "◇" NAIRAS values for date/time/location, black "∗" ARMAS statistical mean values for locations and geomagnetic conditions). These three background estimates lie nearly on top of one another and represent a consensus for the GCR contribution to the radiation environment. From the plane's perspective, which was flying at a constant altitude in this mesoscale region, the increased dose rate for 33 minutes was analogous to flying through a radiation cloud.

In previous work [Tobiska *et al.,* 2016; 2018] it was observed that the dose rate enhancements in these types of measurements were not SEP-related since no solar event had occurred within the previous few hours to days. In addition, changes in GCRs do not normally produce these magnitudes of short-term and localized variability along a flight path. There were no large tropospheric storms or hurricanes in the regions that might produce terrestrial γ-ray flashes (TGFs) or sprites [Chilingarian *et al.,* 2015] as a radiation source. Mertens *et al.* [2010a] show that high geomagnetic activity can affect the aviation radiation environment. However, Tobiska *et al.* [2016] identified only minor Dst disturbances during the events. Because there was essentially no change in background GCRs during each of the ARMAS events during their short durations and there were no SEPs at the time of each event, and because the events demonstrate dynamic variability above the background GCR level over short time scales and across mesoscale regions, these events must be connected to magnetospheric processes.

Substorm injections can provide a source of MeV electrons in the outer radiation belt and are associated with high speed streams (HSS) of particles from the Sun [Tsurutani *et al.,* 2006; Hajra *et al.,* 2015a, 2015b]. Direct injection of MeV particles by substorms has also been reported [Ingraham *et al.,* 2001]. Exploring the 03 October 2015 magnetospheric response, as reflected by geomagnetic activity on this day peaking at Kp = 3+, the Dst index was –24 nT at the time of the event. No solar energetic proton events were reported during this period and no enhancements were detected in either the NOAA GOES >10 MeV proton flux measurements or the Global Positioning System (GPS) proton data. The GOES-13 0.6 MeV electrons were rising and the >1 MeV proton flux was elevated following a rapid enhancement during the 03 October 2015 observations. The >1 MeV protons showed a dispersed substorm particle injection, while the electrons show an enhanced flux following the injection. During geomagnetic substorms, convection strengthens vary quickly across the entire magnetosphere [Miyashita *et al.,* 2008] and the rapid enhancement in GOES-13 1 MeV protons is consistent with their injection to at least geosynchronous orbit. Substorm particle injections, even when they are small, can contribute significantly to radiation belt disturbances [Forsyth *et al.,* 2016; Tang *et al.,* 2016; Tsurutani *et al.,* 2016] and are conducive to wave-particle interactions such as EMIC growth and subsequent relativistic electron precipitation [Blum *et al.,* 2015].

As an example of wave-particle perturbations, EMIC waves can create populations of electrons that are able to precipitate into the atmosphere. Gaines *et al.* [1995] found from UARS HEP measurements that there were 2 orders of magnitude increase in >1 MeV electrons at L = 4 during geomagnetic storm periods followed by significant increases in relativistic electrons in the inner radiation belt ($2 \leq L \leq 3$) a day later. High fluxes of relativistic electrons existed at least a week after a major geomagnetic storm, even while Dst was –30 to –20 nT, and they concluded that ion pair production below 60 km can easily be an order of magnitude more than during quiet geomagnetic conditions. Clilverd *et al.* [2007] were further able to demonstrate dayside relativistic electron precipitation (REP) from EMIC waves, originating in the $4 \leq L \leq 5$ outer radiation belt that were associated with a CME-magnetosphere coupled event. Xu *et al.* [2018] studied monoenergetic beams of 0.1–10 MeV precipitating electrons into the atmosphere to understand the process of bremsstrahlung radiation and its resultant ionization production and atmospheric

effects, including pitch angle dependence in the ionization rate profile. EMIC waves can be ducted through the ionosphere before reaching the ground [Kim *et al.,* 2011], thus allowing for their observations by ground-based magnetometers far from the field lines where they originate [Rodger *et al.,* 2007].

An important feature contributing to electron precipitation losses is the spread in their pitch angle distribution. Electrons with a wide range of equatorial pitch angles can bounce (mirror) from one conjugate hemisphere to the other as they drift between magnetic field lines. However, EMIC waves will modify the pitch angles such that more electrons find their pitch angles pushed towards the loss cone leading to atmospheric loss (precipitation) of the particle. While EMIC waves may be generated in the midnight sector of the magnetosphere during substorm particle injections, it is typical for wave growth to occur that results in transport of relativistic electrons to the dayside magnetosphere within minutes. The peak of ARMAS measured events, made almost exclusively in daytime sector L-shells, were on this time scale.

Once the relativistic electrons hit the top of the atmosphere, considered to be between 50–100 km, bremsstrahlung and other processes can occur. From *electron* impact bremsstrahlung produces a γ-ray (1.24–124 MeV) or X-ray (0.124–1.24 MeV) [IS:21348, 2007] photon. Those high-energy *photon* can then induce one of the following ionizing processes: *i)* the photoelectric effect to produce an electron; *ii)* Compton scattering to eject a secondary inner shell (lower energy) electron plus a photon; or *iii)* pair production to eject a secondary inner shell electron plus a positron that then decays to an electron and photon. Thus, relativistic electron impacts on mesospheric and stratospheric N_2 and O_2 can cause production of lower energy secondary photons and electrons. The resultant spray of these secondaries and tertiaries can then impact other atmospheric target atoms causing additional lower energy photons and particles. Artamonov *et al.* [2016], using the CRAC:EPII model, have even demonstrated ion pair production in the lower atmosphere between 155–205 g cm^{-2} (12–10 km) due to >10 MeV primary electrons producing secondary radiation.

2.5 Magnetospheric transport

Lower energy cosmic rays are effectively attenuated by the geomagnetic field (internal field plus magnetospheric contributions) as these charged particles are transported through the magnetosphere and into the neutral atmosphere. The geomagnetic field provides a form of momentum shielding, or attenuation, by deflecting the lower-energy charged particles back out to space via the Lorentz force. This spectral filtering effect is quantified by a canonical variable, in the mathematical sense, called the geomagnetic cutoff rigidity, R_c. Once the cutoff rigidity is known, the minimum access energy to the neutral atmosphere is determined for each incident charged particle through the relativistic energy equation [Mertens *et al.,* 2010a].

The geomagnetic cutoff rigidity quantity is determined by considering the motion of a charged particle in a magnetic field. The particle motion is solved with Newton's equation of motion for a charged particle subject to the Lorentz force. For a positively charged particle, the equation of motion is

$$d\boldsymbol{p}/dt = (Ze/c)\ \mathbf{v} \times \mathbf{B} \qquad (8)$$

in cgs units. The bold-faced quantities are vectors and × designates the vector cross product. The charged particle momentum and velocity are $\boldsymbol{p}$ and $\boldsymbol{v}$, respectively, and $\mathbf{B}$ is the magnetic field strength. The magnitude of the charge of an electron is denoted e and Z is the number of electron charge units. The equation of motion in (8) can be written, equivalently, as

$$(R/B)\ d\boldsymbol{v}\hat{}/dt = \mathbf{v}\hat{} \times \mathbf{B}\hat{} \qquad (9)$$

where the ˆ symbol denotes unit vectors and

$$R \equiv pc/Ze \tag{10}$$

is defined as the rigidity. The canonical aspect of the rigidity is evident in the above equation. For a given magnetic field strength, **B**, charged particles with the same rigidity follow identical trajectories.

Motions of charged particles in a pure magnetic dipole field were examined by Störmer [1965]. Because of the azimuthal symmetry in a pure dipole field, the azimuthal angular momentum is a conserved quantity. A main feature of Störmer theory is that regions of bounded and unbounded motion can be derived analytically from the integral of motion found from the conservation of azimuthal angular momentum [Störmer, 1965; Van Allen, 1968]. It can be shown that the minimum rigidity that a vertically arriving particle must have in order to reach an altitude z above the Earth's surface is

$$R_{vc} = \frac{\mathcal{M}}{(R_e + z)^2} \cos^4 \lambda_m \approx 15 \cos^4 \lambda_m \,(\mathrm{GV}). \tag{11}$$

In the above equation, R_{vc} designates the vertical geomagnetic cutoff rigidity, M is the Earth's magnetic dipole moment, Re is the average radius of the Earth, and λ_m denotes magnetic latitude. Therefore, vertically arriving charged particles with energies (E) less than the cutoff energy (E_{vc}) will be deflected by the Lorentz force and not reach altitude z. The cutoff energy for each charged particle of charge Z and mass number A is determined from the canonical cutoff rigidity through the relativistic energy equation, such that

$$E_{vc} = \left[\sqrt{R_{vc}^2 \,(Z/A \cdot \mathrm{amu} \cdot c^2)^2 + 1} - 1\right] \cdot \mathrm{amu} \cdot c^2, \tag{12}$$

where E is kinetic energy per nucleon (MeV/n), R_{vc} is vertical geomagnetic cutoff rigidity (MV), c is the speed of light in vacuum, and amu = 931.5 MeV/c^2 (atomic mass unit). Thus, the geomagnetic field has the effect of filtering out lower-energy charged particles as they are transported through the magnetosphere and into the neutral atmosphere.

The vertical cutoff rigidity at the Earth's surface derived from Störmer theory is plotted versus geographic latitude in Figure 7. The maximum cutoff rigidity is at the equator since a vertically arriving charged particle is perpendicular to the dipole magnetic field lines at the equator. The effect of the vector cross product in the Lorentz force in (8) is that charged particle motions perpendicular to magnetic field lines will experience the maximum deflection while particle motions parallel to the magnetic field will experience no deflecting force whatsoever. Figure 7 illustrates that a vertically arriving proton at the equator must have a kinetic energy of ~15 GeV to arrive near the surface of the Earth. In the polar regions, vertically arriving charged particles travel parallel to the magnetic field lines. Therefore, the cutoff rigidity is zero and particles of all energies can arrive on the Earth's surface at the magnetic poles.

The Earth's magnetic field is not a pure dipole field. On the contrary, the internal field is comprised of dipolar and non-dipolar contributions [Langlais and Mandea, 2000]. The dipole moment is off-center and tilted with respect to the rotational axis. Furthermore, the magnetic field is distorted at large radial distances ($r \geq 4Re$) by its interaction with the solar wind. A balance between the solar wind dynamic pressure and the magnetic field pressure, from the internal magnetic field, is established by inducing five magnetospheric magnetic field current systems [Tsyganenko, 1989; 2002]. These current systems generate their own magnetic fields which add vectorally to the internal magnetic field. The complexities of the actual internal magnetic field, with dipolar and non-dipolar contributions, and the magnetospheric magnetic field contributions prohibit an

analytical solution for the vertical geomagnetic cutoff rigidity and numerical methods must be employed.

The internal magnetic field can be specified by the International Geomagnetic Reference Field (IGRF) model [Langlais and Mandea, 2000]. In the IGRF, the internal field is represented by a magnetic potential function (ΦM(r, θ, φ, t)). Outside of the internal source region, i.e, for r ≥ Re, the magnetic potential function must be a solution of the Laplace equation. In spherical coordinates, this solution is expressed in the following form:

$$\Phi_M(r,\theta,\phi,t) = R_e \sum_{n=1}^{N} \sum_{m=0}^{n} \left(\frac{R_e}{r}\right)^{n+1} [g_n^m(t) \cos\, m\phi + h_n^m(t) \sin\, m\phi]\, P_n^m(\cos\theta). \qquad (13)$$

In the above equation, r denotes the radial distance from the center of the Earth, θ and φ denote the geocentric colatitude and longitude at a given location. Schmidt-normalized associated Legendre functions of degree n and order m are denoted by Pnm(cos θ), and gnm and hmn denote the Gauss coefficients. The magnetic field components are given by the gradient of the potential function, such that

$$B_r = \frac{\partial \Phi_M}{\partial r},\ B_\theta = \frac{1}{r}\frac{\partial \Phi_M}{\partial \theta},\ B_\phi = \frac{1}{r\sin\theta}\frac{\partial \Phi_M}{\partial \phi}. \qquad (14)$$

The Gauss coefficients are derived from a global set of magnetic field measurements, using the method of least-squares, and are updated every five years by IAGA Division 5 [Langlais and Mandea, 2000; ISO IS 16695:2013]. Secular variations in the Gauss coefficients are also derived from magnetic field measurements so that derivatives of the Gauss coefficients can be computed. In this way, the temporal dependence of the internal geomagnetic field is represented by

$$g_n^m(t) = g_n^m(T_0) + \dot{g}_n^m(t - T_0) \qquad (15)$$

$$h_n^m(t) = h_n^m(T_0) + \dot{h}_n^m(t - T_0) \qquad (16)$$

where the second terms in (15) and (16) include first-order derivatives of the Gauss coefficients. The epoch of the IGRF model is denoted by T_0 and t is such that $T_0 \le t \le T_0 + 5$, where time is expressed in decimal years.

The vertical cutoff rigidities in a realistic magnetic field are determined by numerical solutions of charged particle trajectories in the field using the techniques advanced by Smart and Shea [1994; 2005]. Figure 8 shows the vertical cutoff rigidities at 20 km in the internal IGRF field. The longitudinal variations in the cutoff rigidity are due to a combination of geocentric offset and relative tilt of the magnetic dipole, with respect to the rotational axis, and the non-dipolar contributions to the internal magnetic field. A zonal-average of the IGRF cutoff rigidities in Figure 8 are compared to the analytical Störmer theory in Figure 7. The simple Störmer theory represents the latitudinal behavior of the vertical cutoff rigidity quite well. The displacement of the Störmer theory cutoffs in Figure 7 relative to the numerical solutions of the cutoffs in the IGRF field is due to the fact that the true dipole contribution to the internal magnetic field is off-centered and tilted with respect to the rotational axis.

Models such as NAIRAS using real-time magnetic cutoff rigidities compute them from numerical solutions of charged particle trajectories in a dynamically varying magnetic field that includes both the internal and the magnetospheric magnetic fields (combined, they are called the geomagnetic field) contributions [Kress *et al.,* 2010; Mertens *et al.,* 2009; 2010a]. The cutoff rigidity code was developed by the Center for Integrated Space Weather Modeling (CISM) at Dartmouth College. The CISM-Dartmouth geomagnetic cutoff model can be run using several different empirical, semi-physics-based, and physics-based models [Kress *et al.,* 2004]. In particular, the specification of the geomagnetic field due to Earth's internal field source is provided by the IGRF model

[Langlais and Mandea, 2000]. The real-time dynamical response of the magnetospheric magnetic field to solar wind conditions and IMF can be provided by the semi-physics-based TS05 model [Tsyganenko and Sitnov, 2005], or by the Lyon-Feder-Mobarry (LFM) global MHD (magnetohydrodynamic) simulation code [Fedder and Mobarry, 2004]. Routines are often developed and tested to couple the geomagnetic cutoff model with the different magnetic field models.

As an example, the LFM MHD code may be run as a stand-alone model or coupled with other geospace models. The LFM magnetospheric magnetic fields may be coupled with the Thermosphere-Ionosphere Nested Grid (TING) model [Wang *et al.,* 2004] and/or with the Rice Convection Model (RCM) [Toffoletto *et al.,* 2004], which models the ring current. The semi-physics-based TS05 model provides more accurate cutoff rigidities than the stand alone LFM MHD model, as determined by comparisons with satellite observations during a Halloween 2003 geomagnetic storm.

Figure 9 shows the vertical cutoff rigidity over the northern hemisphere for three different models of the geomagnetic field during the Halloween 2003 storm period. The left column is cutoff rigidity computed using the IGRF field. Since total flight-path exposure at aviation altitudes do not change significantly (<1%) for cutoffs less than 0.05 GV, the cutoffs are set to zero at geographic locations poleward of the 0.05 GV contour (see the bold-white 0.05 GV color contour in Figure 9). The middle column in Figure 9 shows the cutoff rigidities computed using the TS05 field under geomagnetically quiet conditions, October 28 (0200 UT), prior to the onset of the Halloween 2003 SEP event. One can see that even during magnetically quiet conditions, the cutoff rigidities predicted from the TS05 field are lower than predicted from the IGRF field, and the polar cap region (i.e., inside the bold-white 0.05 GV contour in Figure 9) is expanded to lower latitudes. A weaker field predicted by the TS05 model, compared to IGRF, is due in part to the diamagnetic effect of the magnetospheric ring current included in the TS05 model. Lower cutoff rigidities correspond to less momentum shielding and higher radiation exposure levels. The right column in Figure 9 shows the cutoff rigidities during peak geomagnetic storm conditions, October 29 (2100 UT), during SEP event. The cutoffs are lower at all latitudes compared to the two previous simulations, and the polar cap region has expanded to much lower latitudes than during the magnetically quiet period.

An important aspect of these model studies is the change in cutoff rigidity due to the magnetospheric field effect on atmospheric radiation exposure and the identification of accurate and computationally efficient geomagnetic cutoff rigidity models with solar wind-magnetospheric dynamical responses. The ~1 GV suppression in cutoff at mid-latitudes during a geomagnetic storm means that high-level SEP radiation exposure normally confined to the polar cap region will be extended to mid-latitudes.

2.6 Atmosphere transport

The atmosphere absorbs most of the precipitating charged particles, particularly below the mesopause near 85 km. The particles' interaction is predominantly with neutral N_2 and O_2. Collisions with these target molecules create lower energy secondary and tertiary particles as well as photons. If the primary charged particle has enough energy, there will be many generations of secondary particles, called a shower (Figure 1). The secondaries include neutrons (n), p^+, e–, e^+, α (and other nuclear fragments), pions (π), muons (μ), γ-rays, and X-rays. Under typical GCR-dominated conditions when there is no SEP contribution to atmospheric ionizing radiation the primary particles lose energy, the secondary population increases, and the total ionization increases until a maximum ionization rate occurs by 20 km (65,000 ft) called the Regener-Pfotzer maximum

[Regener and Pfotzer, 1935]. When there are increased SEPs, the relatively high flux and low average energy of the SEP particles compared to GCRs can move the Regener-Pfotzer maximum to higher altitudes even though RBPCPs can penetrate down to 10 km. Below the Regener-Pfotzer maximum down to the Earth's surface, the ionization rate continues to decrease because particles and photons are absorbed in an increasingly thick atmosphere. All of these particles are able to collide with an aircraft hull and its interior components, people, or fuel to further alter the radiation spectrum that affects tissue and avionics [IARC, 2000; UNSCEAR, 2000].

There is a strong altitude dependence upon atmospheric shielding. The exposure rate altitude dependence can be used as a risk management tool by the aviation community, since radiation exposure can be significantly reduced by descending to lower altitudes. The exposure rate increases on average by 160% per km between 5 km and 11 km. Between 11 km and 15 km, the exposure rate increases on average by approximately 75% per km. Another canonical way of looking at atmospheric shielding is that there is a doubling of dose rates every 2 km (6500 ft) higher or a halving of dose rates every 2 km lower.

The transport of charged particles through the neutral atmosphere is described by a coupled system of linear, steady-state Boltzmann transport equations, which can be derived on the basis of conservations principles [Wilson *et al.,* 1991]. The transport equation for the directional fluence $\varphi_j(x, \Omega, E)$ of particle type *j* is given by [Mertens et al., 2008; 2007a]

$$\Omega \bullet \nabla \Phi_j(\mathbf{x}, \Omega, E) = \sum_k \int \int \sigma_{jk}(\Omega, \Omega', E, E') \Phi_k(\mathbf{x}, \Omega', E') d\Omega' dE' - \sigma_j(E) \Phi_j(\mathbf{x}, \Omega, E) \qquad (17)$$

where $\sigma_j(E)$ and $\sigma_{jk}(\Omega,\Omega',E,E')$ are the projectile-target macroscopic interaction cross sections. The $\sigma_{jk}(\Omega,\Omega',E,E')$ are double-differential particle production cross sections that represent all processes by which type *k* particles moving in direction Ω' with energy E' produce a particle of type *j* moving in direction Ω with energy E, including radioactive decay processes. The total interaction cross section $\sigma_j(E)$ for each incident particle type *j* is

$$\sigma_j(E) = \sigma_{j,at}(E) + \sigma_{j,el}(E) + \sigma_{j,r}(E), \qquad (18)$$

where the first term refers to projectile collisions with atomic electrons of the target medium, the second term refers to elastic ion-nucleus scattering, and the third term contains all relevant nuclear reactions. The corresponding differential cross sections are similarly ordered.

Consider the transport of GCR and SEP ions through the atmosphere. In this case, the second term in (18) represents elastic ion-nucleus Coulomb scattering between the incident ions and the atoms that comprise the neutral atmosphere. Figure 10 shows the characteristic elastic scattering length versus kinetic energy of various ions colliding with the neutral atmosphere [Mertens *et al.,* 2008]. Ion-nucleus scattering becomes important in the atmosphere only at low energies. For example, the length of the Earth's atmosphere in units of areal density is ~ 1000 g/cm2. Thus, Figure 10 shows that cosmic ray ions will not elastically scatter off an atmospheric nucleus before reaching the surface unless the ion kinetic energy is well below 1 MeV/amu. However, ions with kinetic energy less than 1 MeV/amu are stopped via ionization and/or atomic excitation energy loss processes at high altitudes before a scattering event can take place (Figure 11). Multiple Coulomb scattering and coupling with ionization energy loss become important factors in the transport of ions within living tissue [Mertens et al., 2010b; 2007b], which are related to the degree of biological damage inflicted on sensitive components within the living cell. However, for ion transport through the atmosphere, the ion-nucleus scattering term in (18) can be neglected to a good approximation.

The principle mechanism for atomic interactions between the incident ions and the target medium is ionization and/or atomic excitation. This process is represented by the first term in (18). The result of this interaction is the transfer of energy from the projectile ions to the atomic electrons of

the target medium via the Coulomb impulse force. Since the projectile ion mass is much greater than the electron mass, the ion travels essentially in a straight line as it loses energy through ionization of the target medium. The ionization and atomic excitation energies, as well as the energies of ejected orbital electrons, are usually small in comparison to the incident ion kinetic energy. As a result, the ionization energy loss processes by which the projectile ions transfer energy to the target bound and/or ejected orbital electrons can be considered continuous. Because of this so-called continuous slowing down approximation (CSDA), the energy dE which is lost by the incident ion and transferred to the orbital electrons of the target medium by ionization and/or atomic excitation within an element of path dx is given by the stopping power, S, [Tai *et al.,* 1997], i.e.,

$$S = -\frac{dE}{dx} = \frac{4\pi Z_P^2 Z_T e^4}{mv^2} N \left\{ B_0 - \frac{C(\beta)}{Z_T} + Z_P L_P(\beta) + Z_P^2 L_T(\beta) + \frac{1}{2}[G(M_P, \beta) - \delta(\beta)] \right\} \tag{19}$$

where

$$B_0 = \ln\left(\frac{2mc^2\beta^2}{I(1-\beta^2)}\right) - \beta^2. \tag{20}$$

In the above equations, Z_P and Z_T are the projectile ion charge and the number of electrons per target atom, respectively, v is the projectile velocity, c is the speed of light, $\beta = v/c$, N is the density of atoms in the target medium, and I is the mean ionization potential of the target medium. The electron charge and mass are denoted, respectively, by e and m.

The various terms in (19) have the following interpretation [Tai *et al.,* 1997; Wilson *et al.,* 1991; Mertens *et al.,* 2012]. The B_0 term is the high-energy asymptotic limit of the stopping power assuming that the orbital electrons of the target atoms can be treated as essentially free electrons. This requires that the projectile's velocity be much greater than the orbital velocities of the bound atomic electrons, which is an inadequate approximation for inner shell electrons of heavy element target media. The $C(\beta)/Z_T$ term provides a correction for inner shell electrons. The $L_P(\beta)$ term arises from polarization of the target electrons by the incident ion and is referred to as the Barkas effect. The $L_T(\beta)$ is the Bloch term which provides a correction to the assumption that the ejected orbital electrons in an ionization event can be represented as a plane wave for close collisions with the incident ion. The Mott term is denoted by $G(M_P, \beta)$, where M_P is the mass of the projectile ion, which includes a kinetic correction for the recoil of the target nucleus. The $\delta(\beta)$ term is a density correction that originates from the dielectric response of a solid target material to the electric field generated by the projectile ion. Finally, at low energy charge exchange processes begin to dominate, which leads to electron capture by the projectile ion and reduces the atomic excitation and/or ionization energy loss. This effect is included by introducing an effective charge for the projectile ion [Tai *et al.,* 1997].

Figure 12 shows the stopping power for various cosmic ray ions incident on Earth's atmosphere. The stopping power decreases inversely with projectile energy between ~100 keV/amu and 2 GeV/amu. The stopping power begins to increase with increasing projectile energy above 2 GeV/amu due to the relativistic corrections in the B_0 term in (19). The stopping power decreases for projectile energies less than ~100 keV/amu due to electron capture by the projectile ion and the other correction terms in (19). The dependence of the stopping power on the projectile kinetic energy plays a major role in determining the spectral shape of the cosmic ray fluence rates in the atmosphere, as indicated by Figures 13 and 14.

The range of an ion is the mean path length traveled in the target medium before coming to rest after losing its initial kinetic energy through ionization and/or atomic excitation energy loss. In the CSDA, the range is defined by

$$R_j(E) = A_j \int_0^E \frac{dE'}{S_j(E')} \tag{21}$$

where A_j is the atomic mass number of ion particle type *j*. The above equation is referred to as the range-energy relation. Figure 11 shows the range of various ions incident on the neutral atmosphere as a function of ion kinetic energy. At 1 GeV/amu, only protons and alpha particles can reach the typical cruising altitudes of ~10-12 km, or ~200 g/cm^2, for commercial aircraft before coming to rest due to ionization energy loss. Below 1 GeV/amu, all incident ions lose their kinetic energy before reaching commercial aircraft cruising altitudes. For energies greater than 1 GeV/amu, the charged particle flux densities decrease with a power-law dependence on energy (Figure 2). Although secondary charged particles can be produced by nuclear fragmentation reactions, which is represented by the third term in (18), the stopping range in Figure 11 explains why the heavy-ion fluence rates in Figure 13 are significantly less than the proton fluence rate. The same is true for the light-ions in Figure 14.

Two approximations can be made to the total ion-target interaction cross section in (18). First, elastic ion-nucleus scattering has been neglected for cosmic ray transport through the atmosphere. Second, the CSDA has been invoked in the representation of atomic ion-electron energy transfer collisions. As a consequence of these two approximations, the coupled Boltzmann transport equations in (17) can be expressed, alternatively, as

$$\overline{B}[\Phi_j(\mathbf{x},\mathbf{\Omega},E)] = \sum_k \int\int \sigma_{jk,r}(\mathbf{\Omega},\mathbf{\Omega}',E,E')\Phi_k(\mathbf{x},\mathbf{\Omega}',E')d\mathbf{\Omega}'dE' \tag{22}$$

where

$$\overline{B}[\Phi_j(\mathbf{x},\mathbf{\Omega},E)] \equiv \left[\mathbf{\Omega}\bullet\nabla - \frac{1}{A_j}\frac{\partial}{\partial E}S_j(E) + \sigma_{j,r}(E)\right]\Phi_j(\mathbf{x},\mathbf{\Omega},E). \tag{23}$$

The $\overline{B}[\Phi_j]$ in the above equations denote a differential operator acting on the directional fluence.

The differential operator in (22) can be inverted using the method of characteristics in order to transform the integro-differential equation into a Volterra-type integral equation [Wilson, 1977]. As a result, the integral equation for cosmic ray transport is given by

$$\begin{aligned}\Phi_j(\mathbf{x},\mathbf{\Omega},E) = {} & \frac{S_j(E_\gamma)P_j(E_\gamma)}{S_j(E)P_j(E)}\Phi_j(\mathbf{\Gamma}_{\mathbf{\Omega},\mathbf{x}},\mathbf{\Omega},E_\gamma) \\ & + \sum_k \int_E^{E_\gamma} \frac{A_j P_j(E')}{S_j(E)P_j(E)}dE' \int_{E'}^{\infty} dE'' \int d\mathbf{\Omega}'\, \sigma_{jk,r}(\mathbf{\Omega},\mathbf{\Omega}',E',E'') \\ & \text{x}\ \Phi_k[\mathbf{x} + (R_j(E) - R_j(E'))\mathbf{\Omega},\mathbf{\Omega}',E'']. \end{aligned} \tag{24}$$

In the above equation, $\Gamma_{\Omega,x}$ is a position vector of a point on the boundary surface and E_γ is given by(25)

$$E_\gamma = R_j^{-1}[R_j + \mathbf{\Omega}\bullet(\mathbf{x} - \mathbf{\Gamma}_{\mathbf{\Omega},\mathbf{x}})] \tag{25}$$

$$P_j(E) \equiv \exp\left[-A_j \int_0^E \frac{\sigma_{j,r}(E')dE'}{S_j(E')}\right].$$

The R_j^{-1} operator in (25) is the inverse operation of obtaining the energy given the range using the range-energy relation in (21). The expression for the integral cosmic ray transport equation in (24) was made compact by introducing the total nuclear

survival probability, which is defined by

(26)

The first term in (24) describes the attenuation of the directional fluence specified at the boundary as a result of transport through the target medium. For atmospheric cosmic ray transport, an isotropic distribution can be assumed for the directional fluence and the boundary specification can be defined as the charged particle fluence rates that have been transported through the heliosphere and magnetosphere and incident at the top of the neutral atmosphere. These incident ions are attenuated by ionization energy loss (S(E)) and nuclear absorption (P(E)), as indicated by the first term in (24). The second term in (24) describes the generation of type *j* particles from projectile-target nuclear fragmentation reactions by type *k* particles. The second term in (24) includes the production of type *j* particles from type *k* particles at all intervening positions between the boundary point and the position of observation, accounting for the attenuation by ionization energy loss and nuclear absorption in between the point of production of a type *j* particle and the observation point.

The representation of the relevant total nuclear absorption cross sections ($\sigma_{j,r}$) and nuclear fragmentation production cross sections ($\sigma_{jk,r}$) cannot be expressed in a simple, compact form such as the stopping power in (19)-(20). Nevertheless, important insight into the influence of nuclear reactions on the atmospheric transport of cosmic rays can be gained by examining the probability of a nuclear reaction as a function of incident ion kinetic energy. The probability of a nuclear reaction is one minus the total nuclear survival probability in (26) (i.e., $1 - P_j(E)$), which is shown in Figure 15. For particles with kinetic energy below 100 MeV/amu, there is a small chance of a nuclear reaction. Recall from Figure 2 that the peak of the incident GCR spectrum is between ~200-500 MeV/amu. At these energies, one out of every two particles will undergo some kind of nuclear reaction. For kinetic energies greater than 1 GeV/amu, nearly every particle will be subject to some type of nuclear reaction. Combining this discussion with the discussion of Figure 11, the only primary incident charged particles that can survive transport through the atmosphere and reach the cruising altitudes of typical commercial aircraft are protons with kinetic energy on the order of 1 GeV or greater. The high-LET particles present at 10-12 km with energies less than 1 GeV/amu are secondary particles created at higher altitudes from nuclear fragmentation reactions, most of which are neutrons.

The coupled cosmic ray integral transport equations in (24) are solved in the NAIRAS model, for example, using NASA LaRC's deterministic HZETRN code. Details of the early analytical and computation approaches to solving (24) are given by Wilson *et al.* [1991; 1995a; 1997; 2005b]. The stopping power parameterization used in HZETRN is described by Tai *et al.* [1997]. The nuclear cross sections for neutron and proton interactions are described extensively in Wilson *et al.* [1989]. The model for calculating the heavy-ion nuclear fragmentation cross sections are described by Wilson *et al.* [1995b; 2005c]. HZETRN is used in a wide variety of radiation transport applications: e.g., the calculation of dosimetric quantities for assessing astronaut risk to space radiations on the International Space Station (ISS) and the Space Transportation System (STS) Shuttle, including realistic spacecraft and human geometry [Badavi *et al.,* 2005; 2007; Slaba *et al.,* 2009; Wilson *et al.,* 2006]. Extensive summaries of HZETRN laboratory and space-flight verification and validation are found in recent reports [Badavi *et al.,* 2007; Nealy *et al.* 2007; Wilson *et al.,* 2005a; 2005c]. In the NAIRAS model, there are 59 coupled transport equations in the HZETRN description of GCR transport through the atmosphere. This set includes transport equations for neutrons and GCR nuclear isotopes from protons through nickel (Z=28, A=58).

Since neutrons do not interact with the target medium via the Coulomb force, there is not an ionization threshold, or an atomic excitation threshold, or a nuclear Coulomb potential barrier to overcome. Thus, the neutrons are not brought to rest as the charged particles are. Neutrons continue to cascade down in energy through neutron-nucleus interactions and the low-energy neutron fluence continues to build, as is evident in Figure 12. The low-energy neutron fluence is quite large, even at a small atmospheric depth of 0.1 g/cm2. The large low-energy neutron fluence at small atmospheric depth is dominated by backscattered neutrons generated at much larger depths, or at much lower altitudes in the atmosphere. At the atmospheric depth of typical cruising altitudes of commercial aircraft, the heavy-ions have largely disappeared, due to a combination of ionization energy loss and nuclear fragmentation reactions into lower energy, lighter particles. Refer to the discussion of Figures 11 and 15.

Solar particles consist mainly of protons and alpha particles. As a result, only the solution of the six light-particle coupled transport equations defined in HZETRN are required in the description of SEP transport through the atmosphere. Similar to the GCR atmospheric transport properties, the large low-energy neutron fluence at small atmospheric depth for SEP events is due to the large backscattered neutron component, which also originates at larger penetrations depths. Furthermore, only nucleon (protons + neutrons) fluences remain at the typical cruising altitude of commercial aircraft, for the same reasons as previously described.

2.7 Radiation dosimetry

Radiation can result in several injury pathways within human tissues by ionizing, dissociating, or exciting atoms and molecules. Pathways include (i) free radical production, (ii) chemical bond breakage, (iii) new chemical bonds production and cross-linkages between macromolecules, and (iv) molecular damage related to regulation of vital cell processes, such as deoxyribonucleic acid (DNA), ribonucleic acid (RNA), and proteins [UNSCEAR, 2000; Tobiska *et al.,* 2017]. High linear energy transfer (LET, i.e., the energy lost by a radiation per unit track length) radiations are typically more harmful to living tissues per unit dose (energy deposited per unit of target mass) than low-LET radiations. Photons, muons, and electrons comprise low-LET radiations, while neutrons, alpha particles, and heavier ions are high-LET radiations. Protons and charged pions can be considered low-LET radiation but interact more like high-LET radiation such that they are treated separately in dosimetry [ICRP, 2008]. Although cells can repair damage from low ionizing radiation doses, higher doses can result in cell death. At extremely high doses, an organ's cell population can rapidly drop and cells may not be replaced quickly enough such that the tissue fails to function normally [IARC, 2000; UNSCEAR, 2000]. These latter effects may be observed when absorbed doses exceed 100 mGy. However, such doses or corresponding dose rates have not been observed from cosmic radiation in the atmosphere. Instead, epidemiological studies in occupational groups conducted over several decades usually focus on long-term effects of radiation-associated cancer [Grajewski *et al.,* 2011].

The energy deposited in a target medium by the radiation field of particle j is the dose, which is given by

$$D_j(\mathbf{x}) = K \int_{\mathbf{\Omega}} \int_0^{\infty} S_j(E) \Phi_j(\mathbf{x}, \mathbf{\Omega}, E) d\mathbf{\Omega} dE. \quad (27)$$

In the above equation, $S_j(E)$ is the target stopping power for particle *j* (Mev/g/cm^2) and K is a unit conversion factor (1.602×10^{-10}) to convert dose to units of Gray (1 Gy = J/kg). The target stopping power is given by (19)-(20), which is shown in Figure 12 for representative cosmic ray ions incident on Earth's atmosphere. Radiation health risk and the probability of biological damage depend not only on the absorbed

$$H_{j,T}(\mathbf{x}) = \int_L Q(L) D_j(\mathbf{x}, L) dL,$$

dose, but also on the particle type and energy of the radiation causing the dose. This is taken into account by weighting the absorbed dose by a factor related to the quality of the radiation. The weighted absorbed dose has been given the name dose equivalent by the ICRP [ICRP, 1991]. The unit of dose equivalent is the Sievert (Sv). Dose equivalent in tissue T from particle *j* (H_j,T(x)) is defined in terms of the tissue LET dependent quality factor, Q, such that

(28)

where L is LET, which can be approximated by the stopping power in units of keV/um; $D_j(x, L)$ is the spectral dose distribution from particle *j* in terms of LET, and Q(L) is the tissue LET-dependent quality factor.

The relationship between the probability of biological damage and dose equivalent is found to also depend on the organ or tissue irradiated. A further dosimetric quantity, called the effective dose, is defined to include the relative contributions of each organ or tissue to the total biological detriment caused by radiation exposure. The effective dose (E(x)) is the sum of weighted dose equivalents in all the organs and tissues in the human body, such that

$$E(\mathbf{x}) = \sum_T \sum_j w_T H_{j,T}(\mathbf{x}). \quad (29)$$

The organ/tissue weighting factors are given in the ICRP 60 report [ICRP, 1991]. A computationally efficient approach is to calculate the effective dose rates directly from the particle spectral fluence rates using pre-computed fluence-to-effective dose conversion coefficients. For example, the NAIRAS model uses neutron and proton conversion coefficients tabulated by Ferrari *et al.* [1997a; 1997b] and the ARMAS derived data use fitted functions [Matthiä *et al.,* 2014; Tobiska *et al.,* 2016]. The effective dose contributions from the other ions are obtained by scaling the proton fluence-to-effective dose conversion coefficients by Z_j^2/A_j, according to stopping power dependence on charge and mass in (19)-(20). All recommended ICRP radiation exposure limits are defined in terms of effective dose.

Figure 16 shows the proton and neutron fluence-to-effective dose conversion coefficients and the event-averaged GCR and SEP spectral fluence rates computed during the Halloween 2003 SEP event. The fluence rates were computed at zero vertical geomagnetic cutoff rigidity at an atmospheric depth of 200 g/cm^2, which is the depth corresponding to typical cruising altitudes of 10-12 km for commercial aircraft. Above 20 MeV, protons make a larger contribution to effective dose per unit fluence compared to neutrons. Below 20 MeV, the reverse is true. The fluence rates are shown in Figure 16 as a product of the fluence rates times the energy. This is a convenient representation on a log-log scale since the spectral integration with respect to log-energy, which is performed in order to obtain the effective dose rate, is proportional to energy multiplied by the fluence rate. In this representation, neutrons dominate below about 1 GeV. The peak in energy times the proton fluence rate is slightly larger for the SEP component as compared to the GCR component. At 100 MeV and below, the energy times the neutron fluence rate is nearly an order of magnitude greater for the SEP component compared to the GCR component.

The GCR and SEP normalized spectral and accumulated spectral effective dose rates are presented in Figure 17 for the event-averaged Halloween 2003 SEP event. Similar to the previous figure, the effective dose rate quantities were computed at zero vertical geomagnetic cutoff rigidity at an atmospheric depth of 200 g/cm^2. The spectral effective dose rates are normalized with respect to the peak in the spectrum. The peak in both the proton and neutron spectral effective dose rates occur between 100-200 MeV, which is true for both GCR and SEP contributions. Neutrons make the largest contributions to effective dose at energies below the peak in the spectrum. Protons make

the largest contribution to effective dose at energies above the peak in the spectrum. The relative spectral contribution of protons and neutrons to effective dose holds for both the GCR and SEP components. Half of the total effective dose rate comes from spectral contributions at energies less than 100 MeV for the GCR component and at energies less than roughly 20 MeV for the SEP component. Half of the neutron effective dose comes from spectral contributions at energies less than about 30 MeV for the GCR component, which is similar for the SEP component. Recall that the incident GCR and SEP proton fluence rates spectra are very different. As a result, half of the proton effective dose rates comes from spectral contributions at energies less than 100 MeV for the SEP component and at energies less than about 500 MeV for the GCR component.

2.8 Avionics

High-energy neutrons (E > 10 MeV) and very low energy thermalized neutrons can cause single event effect (SEE) errors in avionics [Dyer and Lei, 2001; Dyer *et al.,* 2003a; Dyer and Truscott, 1999; Mutuel, 2016; Normand *et al.,* 1994, 2006]. The high-energy neutrons directly interact with silicon (Si) nuclei in electronics through nuclei recoils to produce excess charge carriers. The very low energy neutrons are created by scattering from atmospheric constituents as well as aircraft materials, fuel and, passengers and reach thermal equilibrium in an energy range of 0.02–0.2 eV. They are then absorbed by boron (particularly ^{10}B) often found in Si-based aircraft electronics. After absorption a γ-ray (480 keV) is produced along with an alpha particle (~4 MeV) and a lithium ion. The charged alpha particle is then available to interact with semiconductor structures and may cause a SEE. Higher Z elements near the silicon layers (e.g., tungsten connectors) can increase the SEE effect [Tobiska, *et al.,* 2015]. SEE in avionics is a probabilistic phenomenon and its mitigation is mainly achieved through improved engineering processes (IEC-62396-1). The existing certification is for quiet cosmic ray conditions only and active or extreme space weather conditions are not considered.

2.9 Models

Many models are capable of reporting the aviation radiation environment. They include: AIR [Johnston, 2008], AVIDOS [Latocha *et al.,* 2009; Latocha *et al.,* 2014], CARI-7 [Copeland, 2017], EPCARD.NET [Mares *et al.,* 2009], FDOSCalc [Wissmann *et al.,* 2010], FREE [Felsberger *et al.,* 2009], KREAM [Hwang *et al.,* 2014], NAIRAS [Mertens *et al.,* 2013], PANDOCA [Matthiä *et al.,* 2014], PARMA/EXPACS [Sato *et al.,* 2008; Sato, 2015], and PC-AIRE [McCall *et al.,* 2009]. While all of these models are based on or compared with flight data, the drivers needed for individual models vary. Empirical models like PC-AIRE and FDOSCalc are built from empirical functions fit to in-flight measurement databases representing the GCR environment only. PCAIRE, for example, used the TEPC instrument for assembling its database and is driven by date/time and flight path. These inputs are correlated with GCR-related dose estimates based on the solar cycle, altitude, and magnetic latitudes/longitudes. SEP-related dose can be estimated in post-event analyses. Physics-based models like CARI-7, EPCARD.NET, NAIRAS, and PANDOCA start from the particle spectrum (SEP or GCR local interstellar spectrum, based on measurements) and then propagate the particles through Earth's magnetosphere and atmosphere (or even heliosphere for GCRs). Joyce *et al.* [2014] utilized Monte Carlo simulations of showers coupled to CRaTER measurements [Spence *et al.,* 2010; Schwadron *et al.,* 2012] in deep space to estimate dose rates through the Earth's atmosphere at a range of different altitudes down to aviation heights. Tobiska *et al.* [2018] provided analytical functions to represent the GCR and GCR+REP contributions within the ARMAS flight database, driven by L-shell, NOAA Geomagnetic level, and flight altitude.

The NAIRAS model and ARMAS data have been compared extensively [Tobiska *et al.,* 2018]. NAIRAS is an operational model for predicting aircraft radiation exposure from galactic and solar cosmic rays [Mertens *et al.,* 2010a; 2009; 2008; 2007a]. The real-time exposure rate graphical and tabular data products from the operational prototype stream live from the NAIRAS public web site at http://sol.spacenvironment.net/~nairas/. NAIRAS provides data-driven, global, real-time predictions of atmospheric ionizing radiation exposure rates on a geographic 1x1 degree latitude and longitude grid from the surface of the Earth to 100 km with a vertical resolution of 1 km. The real-time, global predictions are updated every hour. NAIRAS has adopted, as far as possible, the meteorological weather forecasting paradigm of combining physics-based forecast models with data assimilation techniques, i.e., an activity being produced through the NASA *RADIation environment using ARMAS data in the NAIRAS model (RADIAN)* project. Physics-based models are utilized within NAIRAS to transport cosmic rays through three distinct material media: the heliosphere, Earth's magnetosphere, and the neutral atmosphere. While the quantity of observations relevant to radiation exposure predictions is currently too sparse to apply data assimilation techniques per se, nevertheless, as much real-time measurement data as possible are utilized. The real-time measurement data are used to: (1) specify the ionizing radiation field at the boundaries of the aforementioned material media, and (2) characterize the internal properties of the aforementioned material media. The real-time measurements provide necessary observational constraints on the physics-based models that improve simulations of the transport and transmutations of cosmic ray radiation through the heliosphere, magnetosphere, and atmosphere.

There are a number of models currently in use for calculating GCR radiation exposure at aircraft altitudes. The CARI-6 model utilizes a database of transport calculations generated by the deterministic LUIN code for a wide variety of geographic locations, altitudes, and solar activity levels [O'Brien *et al.,* 2003]. The EPCARD model is based on a similar approach but uses the Monte Carlo FLUKA code for the transport calculations [Schraube *et al.,* 1999]. PC-AIRE is a semi-empirical model based on fits to measurement data [Lewis *et al.,* 2002]. Other aircraft radiation exposure models are described in the recent European Radiation Dosimetry Group report [Lindborg *et al.,* 2004]. Currently, the above models calculate SEP atmospheric radiation exposure post-storm on a case-by-case basis, although PC-AIRE incorporated low-earth orbit measurements to develop a simple extrapolation to SEP events [Lewis *et al.,* 2002]. Recently, Copeland *et al.* [2008] calculated adult and conceptus aircraft exposure rates for 170 SEP events for years 1986-2008 using the Monte Carlo MCNPX transport code.

The main differences that distinguish the NAIRAS model from the others includes dynamical solar wind-magnetospheric interactions and the accompanying geomagnetic effects that govern the transport of cosmic rays through the magnetosphere are included in real-time in the NAIRAS radiation exposure calculations [Kress *et al.,* 2004; 2010; Mertens *et al.,* 2010a]. Furthermore, the physics-based deterministic High Charge (Z) and Energy TRaNsport code (HZETRN) is used in transporting cosmic rays through the atmosphere. NAIRAS v2 includes the entire EM cascade in its calculations. The HZETRN transport calculations are continuously updated using real-time measurements of boundary condition specifications of the space radiation environment and of atmospheric density versus altitude [Mertens *et al.,* 2008; 2007a]. And finally, both GCR and SEP atmospheric radiation exposure predictions are included in real-time [Mertens *et al.,* 2010a; 2009].

3 Measurements of the radiation environment

3.1 Instrumentation

Meier *et al.* [2009] have provided a historical overview of dosimetry at aviation altitudes, including the Concorde [Meier, *et al.,* 2016]. Tissue equivalent proportional counters (TEPCs) have been flown with a QinetiQ QDOS/Rayhound spectrometer, the Liulin 4SA, the Eberline FH 41B, and neutron-sensitive bubble detectors [Dyer *et al.,* 2009; Getley *et al.,* 2010] on Boeing 747-400 Qantas Airways flights covering the Northern and Southern Hemispheres (August 2008 to March 2009). Lee *et al.* [2015] used the Liulin detector to measure the dose rate environment over the Korean peninsula on military aircraft. Both the Liulin and Rayhound detectors compared favorably with the TEPC and are within the generally accepted tolerances of 20% [Dyer *et al.,* 2009].

ARMAS has built an extensive database of over a half million one-minute global data records from 8–90 km at all magnetic latitudes and most representative magnetic longitudes. The time frame of ARMAS is a half solar cycle from 2013–2019. This system uses the Teledyne micro dosimeter capturing absorbed dose in silicon [Tobiska *et al.,* 2016; 2018].

An extensive aviation radiation database has been compiled using the Liulin instrument [Ploc *et al.,* 2011; Spurny and Dachev, 2002] on commercial Czech Airlines aircraft since 2001 [Ploc *et al.,* 2013]. The dose rates contain dependencies on flight altitude, geographical position, and solar activity to demonstrate three phenomena: (i) the solar cycle effect upon GCR-induced radiation with higher dose rates seen during solar cycle 23 minimum, (ii) increased geomagnetic cutoff rigidity shielding while moving from high to low geomagnetic latitudes, and (iii) an ability to measure ground-level events while using a continuous monitoring system [Spurny and Dachev, 2001].

Several flight databases have been created during the past decades capturing a wide range of dosimetric measurements. Measurements on aircraft [Dyer *et al.,* 2009, 2003a, 2003b, 2005; Federico *et al.,* 2015; Getley *et al.,* 2010; Iles *et al.,* 2004; Lee *et al.,* 2015; Meier *et al.,* 2009; Meier, *et al.,* 2016a; Ploc *et al.,* 2013; Tobiska *et al.,* 2016, 2018], balloons [Mertens, 2016; Mertens *et al.,* 2016, Tobiska *et al.,* 2018], suborbital vehicles [Tobiska *et al.,* 2018], and the ISS [Dachev, 2017; Dachev *et al.,* 2015, 2017a; b] have provided valuable information. Some of the instruments involved in these campaigns include the following devices.

Tissue equivalent proportional counter (TEPC)

A standard instrument to monitor the radiation dose received by aircraft crews and passengers is the tissue equivalent proportional counter (TEPC). The TEPC instrument is a defacto industry standard and measures energy deposition in simulated volumes that are comparable to those of a living cell [Braby *et al.,* 1994; Gersey, *et al.,* 2002]. The TEPC uses materials and gases that are essentially equivalent to human tissue in chemical composition. Measurements taken with the TEPC are used to calculate radiation dose, radiation quality factor, and dose equivalent. TEPCs have been well characterized in a variety of controlled radiation environments such as particle beam lines and this has provided confidence in their use for operations [Gersey, *et al.,* 2002; Guetersloh *et al.,* 2004; Badhwar *et al.,* 1992]. Energy deposition spectra produced by a TEPC can be used to calculate absorbed dose in tissue and to estimate the average quality factor, Q, of radiation during a flight. A TEPC active volume is a right cylinder where the walls are fabricated

from tissue equivalent A-150 plastic. The right cylinder is enclosed in stainless steel walls. The active volume is then enclosed in an aluminum cylinder, which is referred to as a 'chamber'. The active volume of the TEPC is filled with low-pressure propane gas. An anode wire runs the length of the cylinder and is kept at a potential of 640 volts relative to the cylinder walls. When a high-energy particle enters the TEPC active volume, charge is collected at the anode wire and processed by a pre-amplifier. The signal then moves to a shaping amplifier, is converted into a digital pulse height via an analog to digital converter (ADC) and stored on a flash-ROM card. This information is then translated into lineal energy (the energy deposited in the active volume by a single energy deposition event) is extracted in units of keV/micrometer. A Lineal Energy Transfer (LET) spectrum is created from these measurements and is used to calculate dose equivalent and an average quality factor, Q, of radiation in tissue.

Automated Radiation Measurements for Aerospace Safety (ARMAS)

The difficult task of continuous radiation environment monitoring, reporting, and modeling has not yet been achieved on regional or global scales. There are no existing routine dose measurements at aviation altitudes, either for tissue-relevant or avionics applications. Because of this, the ARMAS program began developing a calibrated, real-time, global monitoring, reporting, and modeling capability of the aviation radiation environment in 2012 [Tobiska *et al.,* 2016].

By spring 2019 ARMAS has obtained real-time radiation measurements from the ground to 90 km for 606 flights consisting of 535678 one-minute measured absorbed dose (silicon) and derived effective dose rate records. The ARMAS monitoring system [Tobiska *et al.,* 2016; 2018] consists of two components: *i)* a flight instrument that measures the environment absorbed dose in silicon on an aircraft and *ii)* a real-time data stream from the aircraft to the ground, which is then processed to Level 4 derived effective dose rates for location and time. Measurements are made using the Teledyne micro dosimeter UDOS001 (μDos) in combination with a microprocessor, a GPS chip, an Iridium transceiver or a Bluetooth transmitter, and associated electronics. The μDos chip is sensitive to heavy ions (Fe^{+}), alphas, protons, neutrons, electrons, and γ-rays, especially above 1 MeV based on extensive ground beam line testing [Tobiska *et al.,* 2016]. All these components are mated to a printed circuit board and housed in a milled aluminum case. Once the absorbed dose (Si) is measured within the aircraft, it is relayed to the ground via Iridium satellite link or aircraft WiFi.

The existing state-of-the-art for real-time total ionizing dose (TID) measurements is the ARMAS Flight Module (FM) instrument, now it its 7^{th} generation. It is manufactured by the Space Environment Technologies and is built for use by research aircraft and suborbital commercial space travel vehicles. The FM uses 5 VDC power from a vehicle-supplied connector passing through a DC-DC converter or with a COTS battery. Total power is 0.5 W (peak), 0.05 W (average), and 0.05 W (standby). It also contains a redundant micro SD data logger. The 1/8" milled aluminum unibody housing contains the electronics. Level 0 engineering units related to absorbed dose in silicon (rad) are integrated in 10-s time-resolved data packets that include UT time tag, latitude, longitude, and altitude. Level 1 dose and Level 2 dose rates in silicon and tissue, as well as Level 3 dose equivalent and ambient dose equivalent rates are provided through an iPhone or iPad app paired with the FM7. The data stream has real-time with 10-second time resolution, no latency, and an ability to store the data inside the app or downlink the data to the ground if the smart device has WiFi connectivity. Level 4 effective dose rates are processed by ground servers and distributed for the benefit of aerospace users. They are available at the ground with 1-minute latency or less. Figure 5 (top panel) shows an example of radiation weather (colored dots) vs. NAIRAS results as well as daily record (black "plus" and "diamond") along with the ARMAS mean statistical database estimate (black "asterisk"). Final data are archived at the

website URL http://sol.spacenvironment.net/armas_ops/Archive/.

Liulin

The Liulin-6SA1 dosimeter spectrometer is well known in the radiation measurement community [Stassinopoulous *et al.,* 2002; Spurny and Dachev, 2003; Dachev, 2013; Dachev *et al.,* 2015] and was used on the RaD-X balloon campaign [Mertens, 2016]. It is manufactured by the Space Research and Technology Institute of the Bulgarian Academy of Sciences in Sofia [Dachev, 2013; Dachev *et al.,* 2015]. The Liulin contains a silicon detector, a charge-sensitive preamplifier, and two micro controllers. The energy deposition of charged particles is measured by pulse height analysis. The pulse amplitudes, following preamplifier processing, is proportional to the energy deposition in the silicon and, thus, to the dose and LET in the ratio 240 mV/MeV. The amplitudes are digitized by an A-to-D converter resulting in a 256- channel spectrum of the energy deposition. The Liulin detects energy in the range of 0.0813–20.8 MeV, corresponding to LET in the silicon detector in the range of 0.27–69.3 keV/μm for perpendicular charged particle flight through the 300 μm thick silicon detector. LET in tissue is lower.

Active Tissue Equivalent Dosimeter (ATED)

The Active Tissue Equivalent Dosimeter (ATED) is a radiation detector built by Oklahoma State University for measuring the LET spectrum, absorbed dose, and biologically weighted dose equivalent of ionizing radiation. The instrument is a gas-filled tissue equivalent proportional counter (TEPC) designed to simulate a 3 μm^3 biological cell; the sensitivity of the detector to ionizing radiation is similar to that of human tissue. A prototype ATED was extensively tested at the Japanese HIMAC calibration facility and at several proton particle accelerators. Currently the ATED is being flown on the ISS. ATED occupies <5000 cm^3 with a mass of <2.5 kg. Total power consumption is <25 Watts. All components except power cable are housed inside an aluminum enclosure. The pressurized detector head is a spherical ionization cavity. A large diameter is used in order to increase the cross-sectional area of the detector to increase the probability of detecting low fluxes of HZE particles. The spherical shell of the proportional counter is made from acrylic ($C_5O_2H_8$) and the inner surface of the shell is made conductive by coating it with colloidal graphite. The detector head is pressurized to 2300 Pa. ATED requires less than 25 Watts of external electrical power. High voltage needed to bias the proportional counter is provided internally by a DC to DC converter. The preamplifier and amplifier circuitry remain unchanged from the original prototype. The signal from the ionization cavity is first impedance-matched by the preamplifier located inside the detector head. The signal is then sent to an operational amplifier and then to a pulse-shaping amplifier before being sent to the spectrometer.

3.2 Campaigns

The NASA *Radiation Experiment* (RaD-X) balloon and aircraft campaign [Mertens, 2016; Meier, *et al.,* 2016b; Tobiska *et al.,* 2016; Norman *et al.,* 2016] collected dosimetric measurements at seven altitudes from 8 to 32 km over 18 h near Fort Sumner, New Mexico, during solar and geomagnetically quiet conditions. The measurements started at commercial aviation altitudes and extended beyond the Regener-Pfotzer maximum. They were taken at similar cutoff rigidities, enabling dosimetric statistical uncertainty to be reduced below 5%. One finding was that protons comprise the dominant contribution from cosmic ray primaries between 21- and 27-km [Norman *et al.,* 2016]. In addition, cosmic ray heavy-ion primaries are discernible at altitudes >32 km.

Recently, the ARMAS database was compared with the NAIRAS model database as part of the

RADIAN project. While ARMAS data were first validated with the RaD-X measurements [Tobiska *et al.,* 2016] the more extensive ARMAS database was encapsulated as polynomial fit equations [Tobiska *et al.,* 2018]. Using equations based on altitude, L shell, and geomagnetic conditions an effective dose rate deriving from a GCR environment can be calculated for any location on the planet. A subset of the ARMAS database was represented by a second polynomial fit equation for the GCR plus probable relativistic energetic particle (REP; Van Allen belt REP) creating Bremsstrahlung γ-ray induced effective dose rates. This subset was contained within a narrow band of L shells ($2 \leq L \leq 6$) combined with altitudinal and geomagnetic dependencies. These databases can help predict the statistically expected radiation environment for regional air traffic management, for airport over-flight operations, and for individual aircraft route planning [Tobiska *et al.,* 2018].

4 Regulatory activities

4.1 International

The Council of the EU adopted Directive 96/20/EURATOM on 13 May 1996. Article 42 of the EU Directive imposes requirements relating to the assessment and limitation of aircrew cosmic ray radiation exposure [AMS, 2007]. EU Member States were required to implement the Directive by 13 May 2000 through national legislation. Consistent with "best practice" radiation protection procedures, which is to keep all radiation exposures as low as reasonably achievable (i.e., the ALARA principle), the EU has also adopted an "action level" of 6 mSv/yr. For those likely to exceed 6 mSv/yr, individual record-keeping and medical surveillance is required of the aircraft operators [Dyer and Lei, 2001]. For exposures less than 6 mSv/yr, only monitoring is recommended and the actual implementation of these recommendation varies among the EU Member States [Meier *et al.,* 2009]. The EU Directive recommendation is that individual exposure is assessed by the aircraft operators if one is likely to exceed 1 mSv/yr, and that workers are educated on radiation health risks and work schedules are adjusted to ensure that the 6 mSv/yr level is not exceeded [EURADOS, 1996].

4.2 U.S.

While there are no U.S. FAA regulations relevant to the radiation environment hazard management at aviation altitudes, the U.S. Space Weather Strategy and Action Plan (SWAP) [National Science and Technology Council, 2015] and White House Executive Order Coordinating Efforts to Prepare the Nation for Space Weather Events [Executive Order 13744, 2016] supported the development and validation of an operational aviation radiation monitoring and forecasting capability. In particular, SWAP sought to (i) identify real-time monitoring requirements of the charged particle radiation environment to protect the health and safety of crew and passengers during space weather events; (ii) define the scope and requirements for a real-time reporting system conveying situational awareness of the radiation environment to orbital, suborbital, and commercial aviation users during space weather events; and (iii) develop or improve models for the real-time assessment of radiation levels at commercial flight altitudes. These Executive Branch initiatives have made their way into Congress where the House and Senate are considering a bill the embodies the elements of SWAP.

5 Conclusions

Air safety improvement from the effects from space weather, and particularly ionizing radiation exposure is a concern faced by aircrew, high-altitude pilots, frequent flyers, and commercial space travelers. This chapter describes the physics of atmospheric radiation, including its primary sources of GCRs and SEPs, as well as an important newly proposed third source, i.e., the secondary radiation environment caused by precipitating radiation belt charged particles.

The GCR primary radiation processes are described, including their transport through the heliosphere and their modulation by the solar wind and changes in the IMF, the modulation connected with the Sun's polar field, their arrival at Earth, and the importance of magnetic shielding by the Earth's geomagnetic field. The SEP primary radiation differential energy spectrum for shock acceleration is described mathematically, and the magnetic shielding by the Earth's geomagnetic field is reinforced. Radiation belt precipitated charged particles, a newer topic in this discipline, is described and data discussed from a new, very large database of atmospheric radiation measurements made by the ARMAS system. The RB source is confined to a band of higher magnetic latitudes mapping to L-shells 2–7.

The transport of charged particles, from any of the three sources, through the magnetic shielding from the Earth's main and magnetospheric magnetic fields, is described and the concept of geomagnetic cutoff rigidity is thoroughly explained, both conceptually and mathematically. The transport of radiation through the atmosphere from precipitating charged particles below the mesopause is presented from a theoretical perspective, including the interactions of neutrons and charged particles with target species in the atmosphere. Radiation dosimetry is described, including the concepts of dose quantities as well as quality factor.

Additional discussions are presented including an introduction on the effects of radiation on avionics, the models capable of reporting the aviation radiation environment, the measurements that have been made of the radiation environment in the atmosphere by specific instruments, and introductory remarks on the regulatory activity internationally and in the U.S. related to the effects of radiation faced by aircrew, high-altitude pilots, frequent flyers, and commercial space travelers.

References

AMS (2007). Integrating space weather observations and forecasts into aviation operations, *Technical report*, American Meteorological Society Policy Program and SolarMetrics.

Artamonov, A. A., A. L. Mishev, and I. G. Usoskin (2016), Model CRAC:EPII for atmospheric ionization due to precipitating electrons: Yield function and applications, *J. Geophys. Res. Space Physics*, *121*, 1736–1743, doi:10.1002/2015JA022276.

Badavi, F. F., Nealy, J. E., de Angelis, G., Wilson, J. W., Clowdsley, M. S., Luetke, N. J., Cuncinotta, F. A., Weyland, M. D. and Semones, E. J. (2005). Radiation environment and shielding model validation for CEV design, *Space 2005*, number AIAA 2005-6651, Am. Inst. of Aeronaut. and Astronaut., Long Beach, California.

Badavi, F. F., Tramaglina, J. K., Nealy, J. E., and Wilson, J. W. (2007). Low earth orbit radiation environments and and shield model validation for ISS, *Space 2007*, number AIAA 2007-6046, Am. Inst. of Aeronaut. and Astronaut., Long Beach, California.

Badhwar, G. D. and O'Neill, P. M. (1991). An improved model of galactic cosmic radiation for space exploration missions, *22nd International Cosmic Ray Conference*, number OG-5.2-13, pp. 643–646.

Badhwar, G. D. and O'Neill, P. M. (1992). An improved model of galactic cosmic radiation for space exploration missions, *Nuclear Tracks Radiat. Meas.,* 20: 403–410.

Badhwar, G.D., A. Konradi, A. Hardy, and L.A. Braby (1992), *Nucl. Tracks Radiat. Meas.*, 20, 13–20.

Badhwar, G. D. and O'Neill, P. M. (1993). Time lag of twenty-two year solar modulation, *23nd International Cosmic Ray Conference*, Vol. 3, pp. 535–539.

Badhwar, G. D. and O'Neill, P. M. (1994). Long term modulation of galactic cosmic radiation and its model for space exploration, *Adv*. *Space Res*. 14: 749–757.

Badhwar, G. D. and ONeill, P. M. (1996). Galactic cosmic radiation model and its applications, *Adv*. *Space Res*. 17: 7–17.

Blum, L. W., A. Halford, R. Millan, J. W. Bonnell, J. Goldstein, M. Usanova, M. Engebretson, M. Ohnsted, G. Reeves, H. Singer, M. Cliverd, and X. Li (2015), Observations of coincident EMIC wave activity and duskside energetic electron precipitation on 18–19 January 2013, Geophys. Res. Lett., 42, 5727–5735, doi:10.1002/2015GL065245.

Braby, L. A., G. D. Badhwar, T. J. Conroy, D. C. Elegy, and L. W. Brackenbush (1994)*, Radiat. Protection Dosimetry*, 52, 423–426.

Brandt, S. (1999). *Data Analysis, Statistical and Computational Methods for Scientists and Engineers*, Springer-Verlag, New York.

Chilingarian, A., S. Chilingaryan, and A. Reymers (2015), Atmospheric discharges and particle fluxes, J. Geophys. Res. Space Physics, 120, 5845–5853, doi:10.1002/ 2015JA021259.

Clem, J., Clements, D. P., Esposito, J., Evenson, P., Huber, D., LHeureux, J., Meyer, P. & Constantin, C. (1996). Solar modulation of cosmic electrons, *Astrophys*. *J*. 464: 507. Clucas, S. N., Dyer, C. S. and Lei, F. (2005). The radiation in the atmosphere during major solar particle events, *Adv*. *Space Res*. 36: 1657–1664.

Clilverd, M. A., C. J. Rodger, R. M. Millan, J. G. Sample, M. Kokorowski, M. P. McCarthy, T. Ulich, T. Raita, A. J. Kavanagh, and E. Spanswick (2007), Energetic particle precipitation into the middle atmosphere triggered by a coronal mass ejection, J. Geophys. Res., 112, A12206, doi:10.1029/2007JA012395.

Copeland, K., Sauer, H. H., Duke, F. E. & Friedberg, W. (2008). Cosmic radiation exposure on aircraft occupants on simulated high-latitude flights during solar proton events from 1 January 1986 through 1 January 2008, *Adv*. *Space Res*. 42: 1008–1029.

Copeland, K., 2017. CARI-7A: development and validation. Radiat. Prot. Dosim. https://doi.org/10.1093/rpd/ncw369.

Dachev, T. P. (2013), Profile of the ionization radiation exposure between the Earth surface and free space, *J. Atmos. Sol. Terr. Phys.,* 102, 148–156.

Dachev, T. P. (2017). Relativistic electron precipitation bands in the outside radiation environment of the international space station. *Journal of Atmospheric and Solar-Terrestrial Physics*, *177*, 247–256. https://doi.org/10.1016/j.jastp.2017.11.008

Dachev, T. P., J. V. Semkova, B. T. Tomov, Yu. N. Matviichuk, P. G. Dimitrov, R. T. Koleva, St. Malchev, N. G. Bankov, V. A. Shurshakov, V. V. Benghin, E. N. Yarmanova, O. A. Ivanova, D. -P. Häder, M. Lebert, M. T. Schuster, G. Reitz, G. Horneck, Y. Uchihori, H. Kitamura, O. Ploc, J. Cubancak, I. Nikolaev (2015), Overview of the Liulin type instruments for space radiation measurement and their scientific results, *Life Sci. Space Res.,* 4, 92-114, doi:10.1016/j.lssr.2015.01.005.

Dachev, T. P., Bankov, N. G., Tomov, B. T., Matviichuk, Y. N., Dimitrov, P. G., Häder, D.-P., and Horneck, G. (2017a). Overview of the ISS radiation environment observed during the ESA EXPOSE-R2 mission in 2014–2016. *Space Weather*, *15*, 1475–1489. https://doi.org/10.1002/ 2016SW001580

Dachev, T. P., N. G. Bankov, B. T. Tomov, Y. N. Matviichuk, P. G. Dimitrov, D.-P. Häder, and G. Horneck (2017b), Overview of the ISS radiation environment observed during the ESA EXPOSE-R2 mission in 2014–2016, Space Weather, 15, 1475–1489. https://doi.org/10.1002/ 2016SW001580.

Dyer, C.S., Truscott, P., 1999. Cosmic radiation effects on avionics. Radiat. Prot. Dosim. 86 (4), 337–342.

Dyer, C. and Lei, F. (2001). Monte Carlo calculations of the influence on aircraft radiation environments of structures and solar particle events, *IEEE Trans. Nucl. Sci.* 48(6): 1987–1995.

Dyer, C. S., Lei, F., Clucas, S. N., Smart, D. F., & Shea, M. A. (2003a). Solar particle enhancements of single event effect rates at aircraft altitudes. *IEEE Transactions on Nuclear Science*, *50*(6), 2038–2045.

Dyer, C. S., Lei, F., Clucas, S. N., Smart, D. F., & Shea, M. A. (2003b). Calculations and observations of solar particle enhancements to the radiation environment at aircraft altitudes. *Advances in Space Research*, *32*(1), 81–93.

Dyer, C., Lei, F., Hands, A., Clucas, S. and Jones, B. (2005). Measurements of the atmospheric radiation environment from cream and comparisons with models for quiet time and solar particle events, *IEEE Trans. Nucl. Sci.* 52(6): 2326–2331.

Dyer, C., Hands, A., Lei, F., Truscott, P., Ryden, K. A., Morris, P., Getley, I., Bennett, L., Bennett, B. and Lewis, B. (2009). Advances in measuring and modeling the atmospheric radiation environment, *IEEE Trans. Nucl. Sci.* 56(8).

Ellison, D. C. and Ramaty, R. (1985). Shock acceleration of electrons and ions in solar flares, *Astrophys. J.* 298: 400–408.

Executive Order 13744 (2016). The White House, executive order—Coordinating efforts to prepare the nation for space weather events, October 13, 2016.

European Radiation Dosimetry Group (EURADOS) (1996). Exposure of air crew to cosmic radiation. A report of EURADOS Working Group 11, *EURADOS Report 1996.01*. In: McAulay, I. R, Bartlett, D. T, Dietze, G. and et al. editors. European Commission Report Radiation Protection 85. Luxembourg: Office for Official Publications of the European Communities.

Fedder, J. G. L. J. A. and Mobarry, C. M. (2004). The Lyon-Fedder-Mobarry (LFM) global MHD magnetospheric simulation code, *J. of Atmos. and Solar-Terrestrial Phys.* 66(15-16): 1333–1350.

Federico, C. A., Gonçalez, O. L., Caldas, L. V. E., Pazianotto, M. T., Dyer, C., Caresana, M., and Hands, A. (2015). Radiation measurements onboard aircraft in the South Atlantic region. *Radiation Measurements*, *82*, 14e20–14e20. https://doi.org/10.1016/j.radmeas.2015.07.008

Felsberger, E., O'Brien, K., Kindl, P., 2009. IASON-FREE: theory and experimental comparisons. Radiat. Prot. Dosim. 136 (4), 267–273. https://doi.org/10.1093/rpd/ncp128.

Ferrari, A., Pelliccioni, M. and Pillon, M. (1997a). Fluence to effective dose conversion coefficients for neutrons up to 10 tev, *Radiat. Prot. Dos.* 71(3): 165–173.

Ferrari, A., Pelliccioni, M. and Pillon, M. (1997b). Fluence to effective dose and effective dose equivalent conversion coefficients for protons from 5 mev to 10 tev, *Radiat. Prot. Dos.* 71(2): 85–91.

Forsyth, C., I. J. Rae, K. R. Murphy, M. P. Freeman, C.-L. Huang, H. E. Spence, A. J. Boyd, J. C. Coxon, C. M. Jackman, N. M. E. Kalmoni, and C. E. J. Watt (2016), What effect do substorms have on the content of the radiation belts?, *J. Geophys. Res. Space Physics,* 121, 6292–6306, doi:10.1002/2016JA022620.

Friedberg, W., Copeland, K. (2003), What aircrews should know about their occupational exposure to ionizing radiation ionizing. Federal Aviation Administration, Civil Aerospace Medical Institute, Oklahoma City, OK. DOT Report No. DOT/FAA/AM-03/16.

Friedberg, W., Copeland, K. (2011), Ionizing radiation in earth's atmosphere and in space near earth. Federal Aviation Administration, Civil Aerospace Medical Institute, Oklahoma City, OK. DOT Report No. DOT/FAA/ AM-11/9.

Gaines, E. E., D. L. Chenette, W. L. Imhof, C. H. Jackman, and J. D. Winningham (1995), Relativistic electron fluxes in May 1992 and their effect on the middle atmosphere, J. Geophys. Res., 100, D1, 1027-1033.

Gaisser, T. (1990). *Cosmic Rays and Particle Physics*, Cambridge University Press.

Getley, I. L., Duldig, M. L., Smart, D. F. and Shea, M. A. (2005a). Radiation dose along north america transcontinental flight paths during quiescent and disturbed geomagnetic conditions, *Space Weather* 3(S01004): doi:10.1029/2004SW000110.

Gersey, B., T. B. Borak, S. Guetersloh, C. Zeitlin, J. Miller, L. Heilbronn, T. Murakami, and Y. Iwata (2002)*, Radiat. Res.*, 157, 350–360.

Getley, I. L., Bennett, L. G. I., Lewis, B. J., Bennett, B., Dyer, C. S., Hands, A. D. P., & Duldig, M. L. (2010). Evaluation of new cosmic radiation monitors designed for aircrew exposure assessment. *Space Weather*, *8*, S01001. https://doi.org/10.1029/2009SW000492

Gopalswamy, N. (2004), A Global Picture of CMEs in the Inner Heliosphere, in *The Sun and the Heliosphere as an Integrated System,* ASSL Series, ed. G. Poletto and S. Suess, Kluwer, Boston, 201.

Grajewski, B., Waters, M. A., Yong, L. C., Tseng, C.-Y., Zivkovich, Z. and Cassinelli II, R. T. (2011). Airline pilot cosmic radiation and circadian disruption exposure assessment from logbooks and company records, *Ann. Occup. Hyg.* 55(5): 465–475.

Guetersloh, S. B., T. B. Borak, P. J. Taddei, C. Zeitlin, L. Heilbronn, J. Miller, T. Murakami, and Y. Iwata (2004)*, Radiat. Res.*, 161, 64–71.

Hajra, R., B. T. Tsurutani, E. Echer, W. D. Gonzalez, and O. Santolik (2015a), Relativistic (E > 0.6, >2.0, and >4.0 MeV) electron acceleration at geosynchronous orbit during high-intensity, long-duration, continuous AE activity (HILDCAA) events, Astrophys. J., 799, 39–46, doi:10.1088/0004-637X/799/1/39.

Hajra, R., B. T. Tsurutani, E. Echer, W. D. Gonzalez, C. G. M. Brum, L. E. A. Vieira, and O. Santolik (2015b), Relativistic electron acceleration during HILDCAA events: Are precursor CIR magnetic storms important?, Earth Planets Space, 67, 109, doi:10.1186/s40623-015-0280-5.

Hwang, J., Dokgo, K., Choi, E., Kin, K.-C., Kim, H.-P., Cho, K.-S., 2014. Korean Radiation Exposure Assessment Model for aviation route dose. In: KREAM, KSS Fall meeting, Jeju, Korea, October 29-31.

Heinrich, W., Roesler, S. and Schraube, H. (1999). Physics of cosmic radiation fields, *Radiat. Prot. Dosim.* 86: 253–258.

ICRP (1991). *ICRP Publication 60: 1990 Recommendations of the International Commission on Radiological Protection*, Vol. 21(1-3), Pergamon Press.

ICRP (2008). *ICRP Publication 103: 2007 Recommendations of the International Commission on Radiological Protection*, ISBN 0-7020-3048-1, Elsevier.

Iles, R. H. A., Jones, J. B. L., Taylor, G. C., Blake, J. B., Bentley, R. D., Hunter, R., et al. (2004). Effect of solar energetic particle (SEP) events on the radiation exposure levels to aircraft passengers and crew: Case study of 14 July 2000 SEP event. *Journal of Geophysical Research*, *109*, A11103. https://doi.org/10.1029/2003JA010343.

Ingraham, J. C., T. E. Cayton, R. D. Belian, R. A. Christensen, R. H. W. Friedel, M. M. Meier, G. D. Reeves, and M. Tuszewski (2001), Substorm injection of relativistic electrons to geosynchronous orbit during the great magnetic storm of March 24, 1991, J. Geophys. Res., 106(A11), 25759–25776, doi:10.1029/2000JA000458.

International Agency for Research on Cancer (2000), Ionizing Radiation, Part 1, X- and γ-Radiation and Neutrons, IARC Work. Group Eval. Carcinog. Risks Hum., vol. 75, IARC and World Health Organization, Lyon, France.

International Standards Organization IS:16695 (2013), Space environment (natural and artificial) — Geomagnetic Reference Models, Geneva.

Johnston, C.O., 2008. A Comparison of EAST Shock-Tube Radiation Measurements With a New Radiation Model. AIAA Paper 2008-1245.

Joyce, C.J., Schwadron, N.A., Wilson, J.K., Spence, H.E., Kasper, J.C., Golightly, M., Blake, J.B., Townsend, L.W., Case, A.W., Semones, E., Smith, S., Zeitlin, C.J., 2014. Radiation modeling in the Earth and Mars atmospheres using LRO/CRaTER with the EMMREM Module. Space Weather 12, 112–119. https://doi.org/10.1002/2013SW000997.

Kahler, S. W. (2001). Origin and properties of solar energetic particles in space, *in* P. Song, H. J. Singer and G. L. Siscoe (eds), *Space Weather*, American Geophysical Union, Washington, DC.

Katsiyannis A.C., M. Dominique, V. Pierrard, G.L. Rosson, J.D. Keyser, D. Berghmans, M. Kruglanski, I.E. Dammasch, and E.D. Donder (2018), The detection of ultra-relativistic electrons in low Earth orbit. J. Space Weather Space Clim. 8: A01.

Kim, H., M. R. Lessard, M. J. Engebretson, and M. A. Young (2011), Statistical study of Pc1–2 wave propagation characteristics in the high-latitude ionospheric waveguide, J. Geophys. Res., 116, A07227, doi:10.1029/2010JA016355.

Kress, B. T., Hudson, M. K., Perry, K. L. and Slocum, P. L. (2004). Dynamic modeling of geomagnetic cutoff for the 23-24 November 2001 solar energetic particle event, *Geophys. Res. Lett.* 31(L04808): doi:10.1029/2003GL018599.

Kress, B. T., Mertens, C. J. and Wiltberger, M. (2010). Solar energetic particle cutoff variations during the 28-31 October 2003 geomagnetic storm, *Space Weather* 8(S05001): doi:10.1029/2009SW000488.

Langlais, B. and Mandea, M. (2000). An igrf candidate geomagnetic field model for epoch 2000 and a secular variation model for 2000-2005, *Earth Planets Space* 52: 1137–1148.

Latocha, M., Beck, P., Rollet, S., 2009. AVIDOS—a software package for European accredited aviation dosim- etry. Radiat. Prot. Dosim. 136 (4), 286. https://doi.org/10.1093/rpd/ncp126.

Latocha, M., Beck, P., B€utikofer, P., Thommesen, H., 2014. AVIDOS 2.0—Current Developments for the Assess- ment of Radiation Exposure at Aircraft Altitudes Caused by Solar Cosmic Radiation Exposure, European Space Weather Week, Liege, 17-21 November. http://stce.be/esww11.

Lee, J., Nam, U.-W., Pyo, J., Kim, S., Kwon, Y.-J., Lee, J., et al. (2015). Short-term variation of cosmic radiation measured by aircraft under constant flight conditions. *Space Weather*, *13*, 797–806. https://doi.org/10.1002/2015SW001288

Lewis, B. J., Bennett, G. I., Green, A. R., McCall, M. J., Ellaschuk, B., Butler, A. and Pierre, M. (2002). Galactic and solar radiation exposure to aircrew during a solar cycle, *Radiat. Prot. Dosim.* 102(3): 207–227.

Lindborg, L., Bartlett, D. T., Beck, P., McAulay, I. R., Schnuer, K., Schraube, H. and (Eds.), F. S. (2004). Cosmic radiation exposure of aircraft crew: compilation of measured and calculated data. a report of eurados working group 5, European Radiation Dosimetry Group, Lexembourg: Office for the Official Publications of the European Communities, European Communities.

Mares, V., Maczka, T., Leuthold, G., Ruhm, M., 2009. Air crew dosimetry with a new version of EPCARD. Radiat. Prot. Dosim. 136 (4), 262–266. https://doi.org/10.1093/rpd/ncp129.

Matthiä, D., Meier, M.M., Reitz, G., 2014. Numerical calculation of the radiation exposure from galactic cosmic rays at aviation altitudes with the PANDOCA core model. Space Weather 12, 161. https://doi.org/ 10.1002/2013SW001022.

McCall, M.J., Lemay, F., Bean, M.R., Lewis, B.J., Bennett, L.G., 2009. Development of a predictive code for aircrew radiation exposure. Radiat. Prot. Dosim. 136 (4), 274–281. https://doi.org/10.1093/rpd/ncp130.

McIlwain, C. E. (1961), Coordinates for Mapping the Distribution of Magnetically Trapped Particles, *J. Geophys. Res., 66*, pp. 3681-3691.

Meier, M., Hubiak, M., Matthiä, D., Wirtz, M. and Reitz, G. (2009). Dosimetry at aviation altitudes, *Radiat*. *Prot*. *Dos*. 136(4): 251–255.

Meier, M.M., Trompier, F., Ambrozova, I., Kubancak, J., Matthi, D., Ploc, O., Santen, N., Wirtz, M., 2016a. CONCORD: comparison of cosmic radiation detectors in the radiation field at aviation altitudes. J. Space Weather Space Clim. 6, A24. https://doi.org/10.1051/swsc/2016017.

Meier, M.M., Matthiä, D., Forkert, T., Wirtz, M., Scheibinger, M., Hübel, R., Mertens, C.J., 2016b. RaD-X: complementary measurements of dose rates at aviation altitudes. Space Weather 14. https://doi.org/10.1002/2016SW001418.

Mertens, C. J. (2016). Overview of the radiation dosimetry experiment (RaD-X) flight mission. *Space Weather*, *14*, 874–898. https://doi.org/10.1002/2016SW001407.

Mertens, C. J., Wilson, J. W., Blattnig, S. R., Solomon, S. C., Wiltberger, M. J., Kunches, J., Kress, B. T. and Murray, J. J. (2007a). Space weather nowcasting of atmospheric ionizing radiation for aviation safety, *45th Aerospace Sciences Meeting and Exhibit*, number AIAA 2007-1104, Am. Inst. of Aeronaut. and Astronaut., Reno, Nevada.

Mertens, C. J., Wilson, J. W., Blattnig, S. R., Kress, B. T., Norbury, J. W., Wiltberger, M. J., Solomon, S. C., Tobiska, W. K. and Murray, J. J. (2008). Influence of space weather on aircraft ionizing radiation exposure, *46th Aerospace Sciences Meeting and Exhibit*, number AIAA 2008-0463, Am. Inst. of Aeronaut. and Astronaut., Reno, Nevada.

Mertens, C. J., Tobiska, W. K., Bouwer, D., Kress, B. T., Wiltberger, M. J., Solomon, S. C. & Murray, J. J. (2009). Development of nowcast of atmospheric ionizing radiation for aviation safety (NAIRAS) model, *1st AIAA Atmosheric and Space Environments Conference*, number AIAA 2009-3633, Am. Inst. of Aeronaut. and Astronaut., San Antonio, Texas.

Mertens, C. J., Kress, B. T., Wiltberger, M., Blattnig, S. R., Slaba, T. S., Solomon, S. C. and Engel, M. (2010a). Geomagnetic influence on aircraft radiation exposure during a solar energetic particle event in October 2003, *Space Weather* 8(S03006): doi:10.1029/2009SW000487.

Mertens, C.J., B.T. Kress, M. Wiltberger, W.K. Tobiska, B. Grajewski, and X. Xu, Atmospheric ionizing radiation from galactic and solar cosmic rays, Current topics in ionizing radiation research, M. Nenoi (Ed.), ISBN: 978-953-51-0196-3, InTech, 2012.

Mertens, C. J., M. M. Meier, S. Brown, R. B. Norman, and X. Xu (2013), NAIRAS aircraft radiation model development, dose climatology, and initial validation, Space Weather, 11, 603–635, doi:10.1002/swe.20100.

Mertens, C. J., Gronoff, G. P., Norman, R. B., Hayes, B. M., Lusby, T. C., Straume, T., et al. (2016). Cosmic radiation dose measurements from the RaD-X flight campaign. *Space Weather*, *14*, 874–898. https://doi.org/10.1002/2016SW001407.

Mewaldt, R. A., Cohen, C. M. S., Labrador, A. W., Leske, R. A., Mason, G. M., Desai, M. I., Looper, M. D., Mazur, J. E., Selesnick, R. S., and Haggerty, D. K. (2005). Proton, helium, and electron spectra during the large solar particle events of october-november 2003, *J. Geophys. Res.* 110(A09S10): doi:10.1029/2005JA011038.

Miyashita, Y., K. Hosokawa, T. Hori, Y. Kamide, A. S. Yukimatu, M. Fujimoto, T. Mukai, S. Machida, N. Sato, Y. Saito, I. Shinohara, and J. B. Sigwarth (2008), Response of large-scale ionospheric convection to substorm expansion onsets: A case study, J. Geophys. Res., 113, A12309, doi:10.1029/2008JA013586.

Mutuel, L.H., 2016. Single Event Effects Mitigation Techniques Report, Department of Transportation/Federal Aviation Administration, TC-15/62, February 2016.

National Science and Technology Council (2015). National Space Weather Action Plan, October 2015.

Nealy, J. E., Cucinotta, F. A., Wilson, J. W., Badavi, F. F., Dachev, T. P., Tomov, B. T., Walker, S. A., Angelis, G. D., Blattnig, S. R. & Atwell, W. (2007). Pre-engineering spaceflight validation of environmental models and the 2005 HZETRN simulations code, *Adv. Space Res.* 4: 1593–1610.

Norman, R. B., Mertens, C. J., and Slaba, T. C. (2016). Evaluating galactic cosmic ray environment models using RaD-X flight data. *Space Weather*, *14*, 764–775. https://doi.org/10.1002/2016SW001401.

Normand, E., Oberg, D.L., Wert, J.L., Ness, J.D., Majewski, P.P., Wender, S., Gavron, A., 1994. Single event upset and charge collection measurements using high energy protons and neutrons. IEEE Trans. Nucl. Sci. 41 (6), 2203–2209.

Normand, E., Vranish, K., Sheets, A., Stitt, M., Kim, R., 2006. Quantifying the double-sided neutron SEU threat, from low energy (thermal) and high energy (>10 MeV) neutrons. IEEE Trans. Nucl. Sci. 53 (6), 3587–3595.

O'Brien, K., O'Brien, K., Smart, D. F., Shea, M. A., Felsberger, E., Schrewe, U., Friedberg, W. and Copeland, K. (2003). World-wide radiation doseage calculations for air crew members, *Adv. Space Res.* 31(4): 835–840.

O'Neill, P. M. (2006). Badhwar-ONeill galactic cosmic ray model update based on advanced composition explorer (ACE) energy spectra from 1997 to present, *Adv. Space Res.* 37: 1727–1733.

Parker, E. N. (1965). The passage of energetic charged particles through interplanetary space, *Planet. Space Sci.* 13: 9–49.

Ploc, O., Pachnerova Brabcova, K., Spurny, F., Malusek, A., & Dachev, T. (2011). Use of energy deposition spectrometer Liulin for individual monitoring of aircrew. *Radiation Protection Dosimetry*, *144*, 611e614.

Ploc, O., Ambrozova, I., Kubancak, J., Kovar, I., & Dachev, T. P. (2013). Publicly available database of measurements with the silicon spectro- meter Liulin onboard aircraft. *Radiation Measurements*, *58*, 107–112. https://doi.org/10.1016/j.radmeas.2013.09.002

Reames, D.V. (2013), The Two Sources of Solar Energetic Particles, Space Sci Rev 175: 53. doi:10.1007/s11214-013-9958-9.

Regener, E. and G. Pfotzer (1935), Vertical Intensity of Cosmic Rays by Threefold Coincidences in the Stratosphere, *Nature,* **136**, 718.

Reitz, G., K. Schnuer, and K. Shaw (1993), Editorial - workshop on radiation exposure of civil aircrew, Radiat. Prot. Dosim., 48, 3.

Rodger, C. J., M. A. Clilverd, N. R. Thomson, R. J. Gamble, A. Seppälä, E. Turunen, N. P. Meredith, M. Parrot, J.-A. Sauvaud, and J.-J. Berthelier (2007), Radiation belt electron precipitation into the atmosphere: Recovery from a geomagnetic storm, J. Geophys. Res., 112, A11307, doi:10.1029/2007JA012383.

Sato, T., 2015. Analytical model for estimating terrestrial cosmic ray fluxes nearly anytime and anywhere in the world: extension of PARMA/EXPACS. PLoS One. 10 (12), e0144679.

Sato, T., Yasuda, H., Niita, K., Endo, A., Sihver, L., 2008. Development of PARMAPHITS-based analytical radiation model in the atmosphere. Radiat. Res. 170, 244.

Schraube, H., Mares, V., Roesler, S. and Heinrich, W. (1999). Experimental verification and calculation of aviation route doses, *Radiat. Prot. Dosim.* 86(4): 309–315.

Schwadron, N.A., Baker, T., Blake, B., Case, A.W., Cooper, J.F., Golightly, M., Jordan, A., Joyce, C., Kasper, J., Kozarev, K., Mislinski, J., Mazur, J., Posner, A., Rother, O., Smith, S., Spence, H.E., Townsend, L.W., Wilson, J., Zeitlin, C., 2012. Lunar radiation environment and space weathering from the Cosmic Ray Tele- scope for the Effects of Radiation (CRaTER). J. Geophys. Res. Planets 117. https://doi.org/ 10.1029/2011JE003978. E00H13.

Simpson, J.A., 1983. Elemental and isotopic composition of the galactic cosmic rays. Annu. Rev. Nucl. Part. Sci. 33, 323–382. https://doi.org/10.1146/annurev.ns.33.120183.001543.

Slaba, T. C., Qualls, G. D., Clowdsley, M. S., Blattnig, S. R., Simonsen, L. C., Walker, S. W., and Singleterry, R. C. (2009). Analysis of mass averaged tissue doses in max, fax, and cam, and caf, *Technical Report TP-2009-215562*, NASA.

Smart, D. F. and Shea, M. A. (1994). Geomagnetic cutoffs: A review for space dosimetry calculations, *Adv. Space Res.* 14(10): 10,787–10,796.

Smart, D. F. and Shea, M. A. (2005). A review of geomagnetic cutoff rigidities for earth-orbiting spacecraft, *Adv. Space Res.* 36: 2012–2020.

Spence, H.E., Case, A., Golightly, M.J., Heine, T., Larsen, B.A., Blake, J.B., Caranza, P., Crain, W.R., George, J., Lalic, M., Lin, A., Looper, M.D., Mazur, J.E., Salvaggio, D., Kasper, J.C., Stubbs, T.J., Doucette, M., Ford, P., Foster, R., Goeke, R., Gordon, D., Klatt, B., O'connor, J., Smith, M., Onsager, T., Zeitlin, C., Townsend, L., Charara, Y., 2010. CRaTER: The Cosmic Ray Telescope for the Effects of Radiation Experiment on the Lunar Reconnaissance Orbiter Mission. Space Sci. Rev. 150 (1-4), 243–284.

Spurny, F., and Dachev, T. (2001). Measurements during an intense solar flare, GLE 60. *Radiation Protection Dosimetry*, *95*, 273e275.

Spurny, F., and Dachev, T. (2002). On board aircrew dosimetry with a semiconductor spectrometer. *Radiation Protection Dosimetry*, *100*, 525e528.

Spurny, F., and T. S. Dachev (2003), Long-term monitoring of the onboard aircraft exposure level with a Si-diode based spectrometer, *Adv. Space Res.,* 32(1), 53–58.

Stassinopoulos, E. G., C. A. Stauffer, T. P. Dachev, G. J. Brucker, B. T. Tomov, and P. G. Dimitrov (2002), The Liulin-3M radiometer for measuring particle doses in space and on aircraft, NASA/TM-2002-210003.

Störmer, C. (1965). *The Polar Aurora*, Oxford at the Clarendon Press. Tai, H., Bichsel, H., Wilson, J. W., Shinn, J. L., Cucinotta, F. A. & Badavi, F. F. (1997). Comparison of stopping power and range databases for radiation transport study, *Technical Report TP-3644*, NASA.

Tai, H., Bichsel, H., Wilson, J. W., Shinn, J. L., Cucinotta, F. A. and Badavi, F. F. (1997). Comparison of stopping power and range databases for radiation transport study, *Technical Report TP-3644*, NASA.

Tang, C. L., J.-C. Zhang, G. D. Reeves, Z. P. Su, D. N. Baker, H. E. Spence, H. O. Funsten, J. B. Blake, and J. R. Wygant (2016), Prompt enhancement of the Earth's outer radiation belt due to substorm electron injections, J. Geophys. Res. Space Physics, 121, 11,826–11,838, doi:10.1002/ 2016JA023550.

Tascione, T.F. (1994), *Introduction to the Space Environment,* 2nd Ed., Krieger Publishing Co., Malabar, FL.

Tobiska, W. K., W. Atwell, P. Beck, E. Benton, K. Copeland, C. Dyer, B. Gersey, I. Getley, A. Hands, M. Holland, S. Hong, J. Hwang, B. Jones, K. Malone, M. M. Meier, C. Mertens, T. Phillips, K. Ryden, N. Schwadron, S. A. Wender, R. Wilkins, M. A. Xapsos (2015), Advances in Atmospheric Radiation Measurements and Modeling Needed to Improve Air Safety, *Space Weather,* ***13,*** 202-210.

Tobiska, W. K., D. Bouwer, D. Smart, M. Shea, J. Bailey, L. Didkovsky, K. Judge, H. Garrett, W. Atwell, B. Gersey, R. Wilkins, D. Rice, R. Schunk, D. Bell, C. Mertens, X. Xu, M. Wiltberger, S. Wiley, E. Teets, B. Jones, S. Hong, K. Yoon (2016), Global real-time dose measurements using the Automated Radiation Measurements for Aerospace Safety (ARMAS) system, *Space Weather,* ***14,*** 1053-1080.

Tobiska, W.K., M.M. Meier, D, Matthiae, and K. Copeland (2017), Characterizing the Variation in Atmospheric Radiation at Aviation Altitudes, *Extreme Events in Geospace,* ed., N. Buzulukova, Elsevier, pp. 453–471, ISBN: 9780128127001.

Tobiska, W. K., L. Didkovsky, K. Judge, S. Weiman, D. Bouwer, J. Bailey, B. Atwell, M. Maskrey, C. Mertens, Y. Zheng, M, Shea, D. Smart, B. Gersey, R. Wilkins, D. Bell, L. Gardner, and R. Fuschino, (2018), Analytical representations for characterizing the global aviation radiation environment based on model and measurement databases. *Space Weather*, *16*. https://doi.org/10.1029/ 2018SW001843.

Toffoletto, F. R., Sazykin, S., Spiro, R. W., Wolf, R. A. and Lyon, J. G. (2004). Rcm meets lfm: initial results of one-way coupling, *J. of Atmos. and Solar-Terrestrial Phys.* 66(15-16): 1361–1370.

Townsend, L. W., Zapp, E. N., Jr., D. L. S. and Hoff, J. L. (2003). Carrington flare of 1859 as a prototypical worst-case solar energetic particle event, *IEEE Trans. Nucl. Sci.* 50(6): 2307–2309.

Townsend, L. W., Stephens, D. L., Hoff, J. L., Zapp, E. N., Moussa, H. M., Miller, T. M., Campbell, C. E. and Nichols, T. F. (2006). The carrington event: Possible doses to crews in space from a comparable event, *Adv. Space Res.* 38: 226–231.

Tsurutani, B. T., W. D. Gonzalez, A. L. C. Gonzalez, F. L. Guarnieri, N. Gopalswamy, M. Grande, Y. Kamide, Y. Kasahara, G. Lu, I. Mann, R. McPherron, F. Soraas, and V. Vasyliunas (2006), Corotating solar wind streams and recurrent geomagnetic activity: A review, J. Geophys. Res., 111, A07S01, doi:10.1029/2005JA011273.

Tsurutani, B. T., R. Hajra, T. Tanimori, A. Takada, R. Bhanu, A. J. Mannucci, G. S. Lakhina, J. U. Kozyra, K. Shiokawa, L. C. Lee, E. Echer, R. V. Reddy, and W. D. Gonzalez. (2016), Heliospheric plasma sheet (HPS) impingement onto the magnetosphere as a cause of relativistic electron dropouts (REDs) via coherent EMIC wave scattering with possible consequences for climate change mechanisms, *J. Geophys. Res. Space Physics,* 121, 10,130–10,156, doi:10.1002/2016JA022499.

Tsyganenko, N. A. (1989). Determination of magnetic current system parameters and development of experimental geomagneitc field models based on data from imp and heos satellite, *Planet Space Sci.* 37: 5–20.

Tsyganenko, N. A. (2002). A model of the near magnetosphere with dawn-dusk asymmetry: 1. mathematical structure, *J. Geophys. Res.* 107(A8): 1179. doi:10.1029/2001JA000219.

Tsyganenko, N. A. and Sitnov, N. I. (2005). Modeling the dynamics of the inner magnetosphere during strong geomagnetic storms, *J. Geophys. Res.* 110: A03208. doi:10.1029/2004JA010798.

Tylka, A. J., Cohen, C. M. S., Dietrich, W. F., Lee, M. A., Maclennan, C. G., Mewaldt, R. A., Ng, C. K. and Reames, D. V. (2005). Shock geometry, seed populations, and the origin of variable elemental composition at high energies in large gradual solar particle events, *ApJ.* 625: 474–495.

Tylka, A. J. and Lee, M. A. (2006). Spectral and compositional characteristics of gradual and impuslive solar energetic particle events, in solar eruptions and energetic particles, *in* N. Gopalswamy, R. Mewaldt and J. Torsi (eds), *Solar Eruptions and Energetic Particles*, Vol. Geophysical Monograph 165, American Geophysical Union, Washington, DC.

United Nations Scientific Committee on the Effect of Atomic Radiation (2000), Sources and effect of ionizing radiation, United Nations Scientific Committee on the Effect of Atomic Radiation UNSCEAR 2000 Report to the General Assembly, with Scientific Annexes, Vol. II, Annex G.

UNSCEAR (1988). *UNSCEAR 1988 Report to the General Assembly: Sources, effects, and risks of ionizing radiation*, number E.88.IX.7, United Nations Scientific Committee on the Effects of Atomic Radiation, United Nations, New York.

VanAllen, J. A. (1968). *Physics of the Magnetosphere*, Vol. 10, Springer-Verlag, New York, New York, chapter Particle Description of the Magnetosphere.

Wang, W., Wiltberger, M., Burns, A. G., Solomon, S. C., Killeen, T. L., Maruyama, N. and Lyon, J. G. (2004). Initial results from the coupled magnetosphere- ionosphere-thermosphere model: thermosphere-ionosphere responses, *J. of Atmos. and Solar-Terrestrial Phys.* 66: 1425–1441.

Wilson, J. W. (1977). Analysis of the theory of high-energy ion transport, *Technical Report TN D-8381*, NASA.

Wilson, J. W. (2000). Overview of radiation environments and human exposures, *Heath Phys.* 79(5): 470–494.

Wilson, J. W., Townsend, L. W., Nealy, J. E., Chung, S. Y., Hong, B. S., Buck, W. W., Lamkin, S. L., Ganapol, B. D., Khan, F. and Cucinotta, F. A. (1989). Bryntrn: A baryon transport model, *Technical report*, NASA.

Wilson, J. W., Townsend, L. W., Schimmerling, W., Khandelwal, G. S., Khan, F., Nealy, J. E., Cucinotta, F. A., Simonsen, L. C., Shinn, J. L., and Norbury, J. W. (1991). Transport methods and interactions for space radiation, *Technical Report RP-1257*, NASA.

Wilson, J. W., Badavi, F. F., Cucinotta, F. A., Shinn, J. L., Badhwar, G. D., Silberberg, R., Tsao, C. H., Townsend, L. W. & Tripathi, R. K. (1995a). HZETRN: Description of a free-space ion and nucleon transport and shielding computer program, *Technical Report TP 3495*, NASA.

Wilson, J. W., J. E. Nealy, F. A. Cucinotta, J. L. Shinn, F. Hajnal, M. Reginatto, P. Goldhagen (1995b), Radiation safety aspects of commercial high-speed flight transportation, NASA Tech. Pap. 3524.

Wilson, J. W., Miller, J. and Cucinotta, F. A. (eds) (1997). *Shielding strategies for human space exploration*, NASA Conference Publication 3360, NASA Johson Space Center.

Wilson, J. W., Joes, I. W., Maiden, D. L. and Goldhagan, P. (eds) (2003). *Analysis, results, and lessons learned from the June 1997 ER-2 campaign*, NASA CP-2003-212155, NASA Langley Research Center.

Wilson, J. W., Mertens, C. J., Goldhagan, P., Friedberg, W., Angelis, G. D., Clem, J. M., Copeland, K. and Bidasaria, H. B. (2005a). Atmospheric ionizing radiation and human exposure, *Technical Report TP-2005-213935*, NASA.

Wilson, J. W., Mertens, C. J., Goldhagan, P., Friedberg, W., Angelis, G. D., Clem, J. M., Copeland, K. & Bidasaria, H. B. (2005b). Atmospheric ionizing radiation and human exposure, *Technical Report TP-2005-213935*, NASA.

Wilson, J. W., Tweed, J., Walker, S. A., Cucinotta, F. A., Tripathi, R. K., Blattnig, S. and Mertens, C. J. (2005c). A benchmark for laboratory exposures with 1 a GeV iron ions, *Adv. Space Res.* 35: 185–193.

Wilson, J. W. and et al. (2006). International space station: A testbed for experimental and computational dosimetry, *Adv. Space Res.* 37: 1656–1663.

Wissmann, F., Reginatto, M., M€oller, T., 2010. Ambient dose equivalent at flight altitudes: a fit to a large set of data using a Bayesian approach. J. Radiol. Prot. 30, 513–524.

Xapsos, M. A., Barth, J. L., Stassionopoulos, E. G., Messenger, S. R., Walters, R. J., Summers, G. P. and Burke, E. A. (2000). Chracterizing solar proton energy spectra for radiation effects applications, *IEEE Trans. Nucl. Sci.* 47(6): 2218–2223.

Xu, W., R. A. Marshall, X. Fang, E. Turunen, and A. Kero, (2018), On the effects of bremsstrahlung radiation during energetic electron precipitation. *Geophysical Research Letters*, *45*, 1167–1176. https://doi.org/10.1002/2017GL076510.

Captions

Fig. 1. The complex radiation conditions at and above commercial aviation altitudes from GCRs and SEPs [Tobiska *et al.,* 2015].

Fig. 2. GCR spectral flux for various nuclei predicted by the Badhwar and O'Neill model for solar cycle 23. The local interstellar spectrum (LIS) is denoted by the red lines. Solar minimum spectra are represented by June 1996 conditions, and are denoted by green lines. Solar maximum spectra are represented by June 2000 conditions, and are denoted by blue lines.

Fig. 3. Solar polar magnetic field data taken by measurements made at the Wilcox Solar Observatory. The light solid blue line is North, the light dashed red line is South, the medium solid black line is average, and the heavy solid black line is the smoothed average of the polar field strength. The '+' and '-' symbols between the vertical dashed lines indicate the time periods of solar positive and negative polarity, respectively.

Fig. 4. ARMAS effective dose rates substantially increase between $4 \leq L \leq 5$ above typical 11 km GCR values for quiet geomagnetic conditions during solar cycle 24 decline.

Fig. 5 The ARMAS 03 October 2015 G5 flight at 11.5 km and magnetic latitudes near –63° with doubled effective dose rate for ~1/2 hour; effective dose rate vs. time compared with NAIRAS (top panel black diamonds) and the flight geographical context with information related to proton cutoff energies and cutoff rigidities (bottom panel).

Fig. 6. One-minute ratios of ARMAS (measurements) to NAIRAS (model; GCR at this time) for all radiation events identified in Table 1, for all altitudes above 8 km, and for geomagnetic conditions of G0 and G1 on the NOAA G-scale. Cutoff rigidities are in units of GV (dashed lines) [Shea and Smart, 2012].

Fig. 7. Zonal-averaged vertical geomagnetic cutoff rigidity. The solid red line corresponds to the quiescent cutoff rigidities computed from particle trajectories and the IGRF model. The green dotted line is the analytical solution for the vertical cutoff rigidity using Störmer Theory.

Fig. 8. Global grid of quiescent vertical geomagnetic cutoff rigidities (GV) calculated from charged particle trajectory simulations using the IGRF model for the 1996 epoch (solar cycle 23 minimum).

Fig. 9. Simulated vertical geomagnetic cutoff rigidity shown over the northern hemisphere in October 2003. The cutoff rigidities in the left column were calculated using the IGRF model. The cutoffs in the middle column were calculated using the TS05 model during a geomagnetically quiet period. Cutoff rigidities in the right column were calculated using the T05 model during the largest geomagnetically disturbed period of SEP event. Also shown are the magnetic latitude circles and the meridians at 0, 6, 12, and 18 magnetic local time.

Fig. 10. Characteristic scattering length for ion beam transport through the Earth's atmosphere. The charge number (z) of the ion is specified in the legend.

Fig. 11. Average range versus kinetic energy of an ion beam incident at the top of Earth's atmosphere. The charge number (z) of the ion is specified in the legend.

Fig. 12. Stopping power versus kinetic energy of incident ions on Earth's atmosphere. The charge number (z) of the ion is specified in the legend.

Fig. 13. Event-averaged GCR spectral fluence rates at zero vertical geomagnetic cutoff rigidity during the Halloween 2003 solar-geomagnetic storm [29 October 2003 (2100 UT) to 1 November (0000 UT)]. The panels show the fluence rates at different atmospheric depths. The typical cruising altitudes for commercial aircraft correspond to an atmospheric depth of roughly 200 g/cm^2. The fluence rates from different charge groups have been summed together to reduce the number of lines.

Fig. 14. Event-averaged SEP spectral fluence rates at zero vertical geomagnetic cutoff rigidity during the Halloween 2003 solar-geomagnetic storm [29 October 2003 (2100 UT) to 1 November (0000 UT)]. The panels show the

fluence rates at different atmospheric depths. The typical cruising altitudes for commercial aircraft correspond to an atmospheric depth of roughly 200 g/cm^2.

Fig. 15. Nuclear survival probability versus kinetic energy of an ion beam incident at the top of Earth's atmosphere. The charge number (z) of the ion is specified in the legend.

Fig. 16. The green lines show the fluence-to-effective dose conversion coefficients. The blue lines show the product of the kinetic energy (MeV/amu) times the event-averaged spectral fluence rates for the Halloween 2003 storm period [29 October (2100 UT) to 1 November (0000 UT)]. The fluence rates were evaluated at zero vertical geomagnetic cutoff rigidity and at an atmospheric depth of 200 g/cm^2. The lines denote neutron quantities; dashed lines denote proton quantities; dotted lines denote alpha quantities. All quantities are shown for: (a) GCR component and (b) SEP component.

Fig. 17. Normalized spectral effective dose rates evaluated during the Halloween 2003 storm period [29 October (2100 UT) to 1 November (0000 UT)] at zero vertical geomagnetic cutoff rigidity and at an atmospheric depth of 200 g/cm^2. The green lines show the spectral effective dose rate normalized to the peak in the spectrum. The blue lines are normalized to the spectrally integrated effective dose rate and show the accumulated effective dose rate as the spectral effective dose rate is integrated over energy. The solid lines denote neutron quantities; dashed lines denote proton quantities; dash-dot lines denote total quantities.

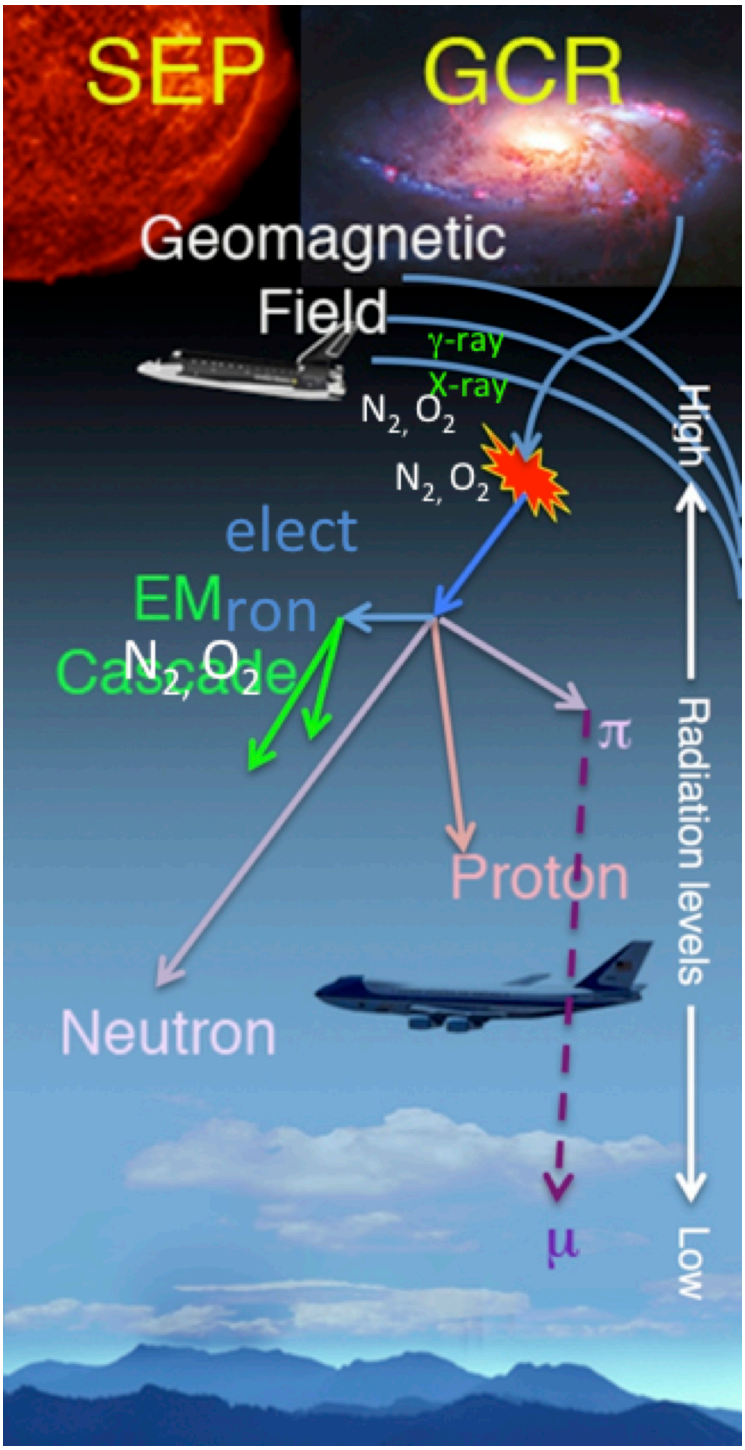

Fig. 1. The complex radiation conditions at and above commercial aviation altitudes from GCRs and SEPs [Tobiska *et al.,* 2015].

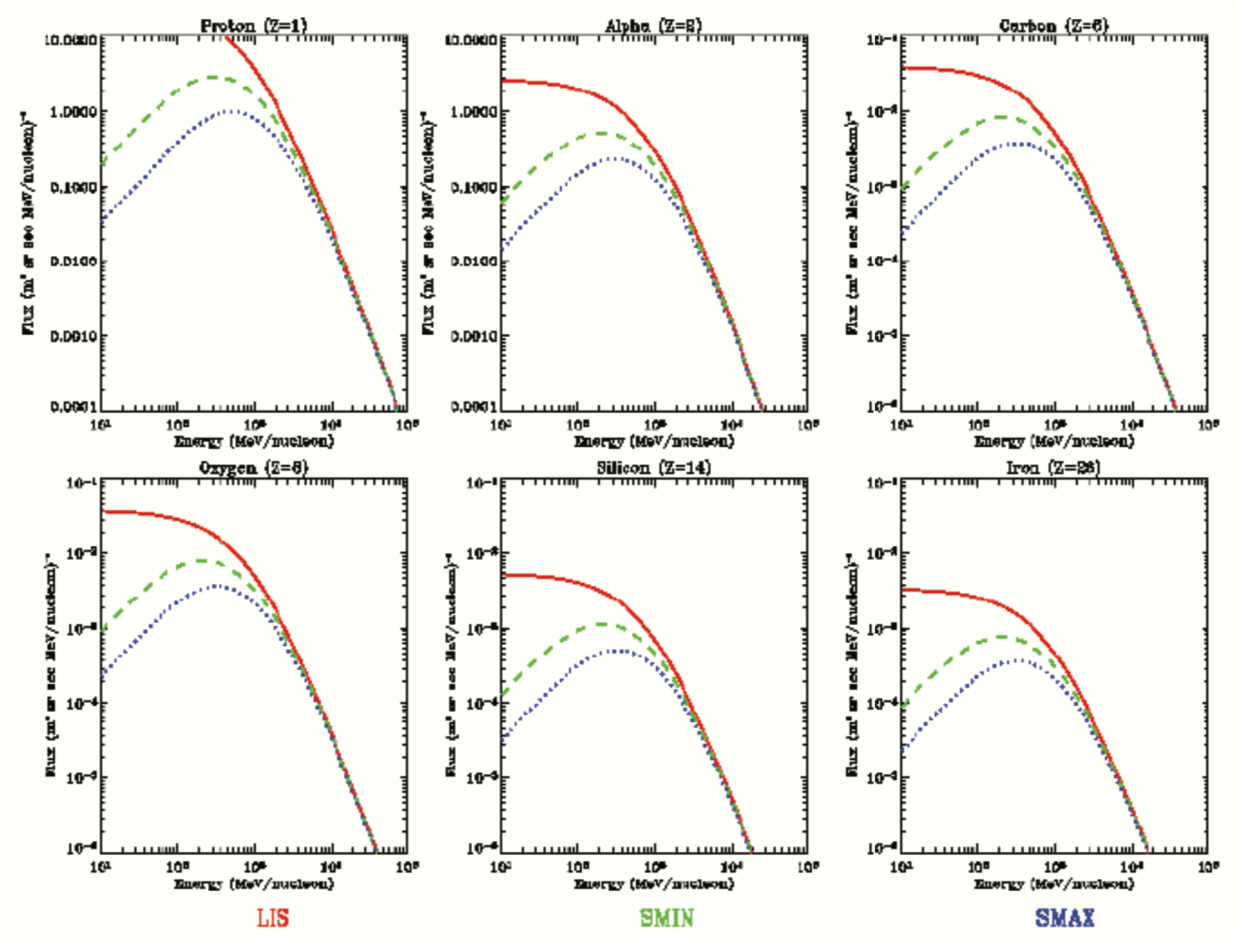

Fig. 2. GCR spectral flux for various nuclei predicted by the Badhwar and O'Neill model for solar cycle 23. The local interstellar spectrum (LIS) is denoted by the red lines. Solar minimum spectra are represented by June 1996 conditions, and are denoted by green lines. Solar maximum spectra are represented by June 2000 conditions, and are denoted by blue lines.

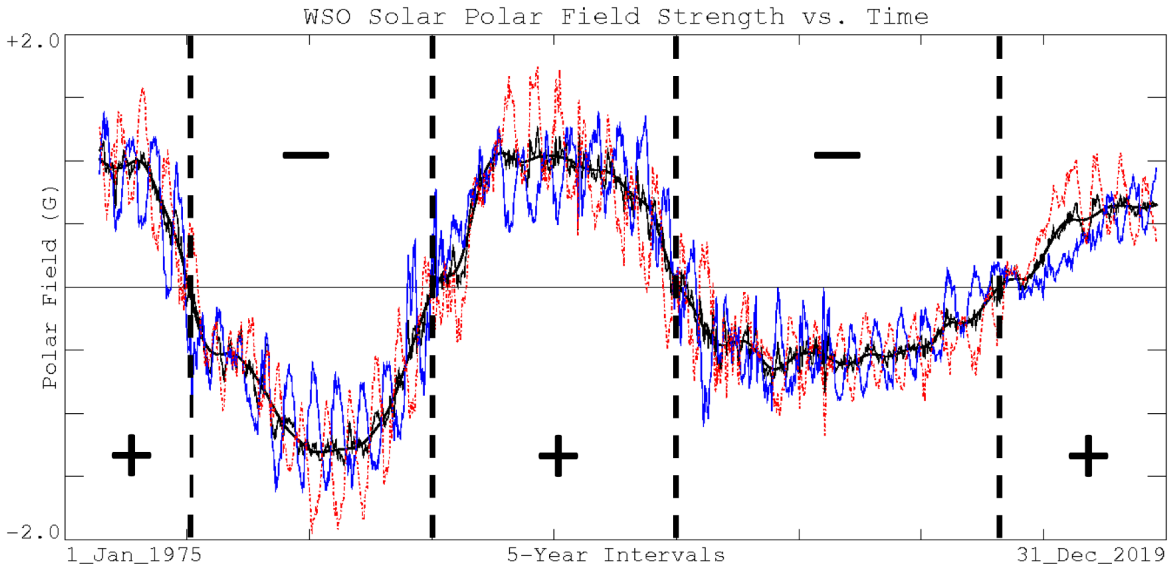

Fig. 3. Solar polar magnetic field data taken by measurements made at the Wilcox Solar Observatory. The light solid blue line is North, the light dashed red line is South, the medium solid black line is average, and the heavy solid black line is the smoothed average of the polar field strength. The '+' and '-' symbols between the vertical dashed lines indicate the time periods of solar positive and negative polarity, respectively.

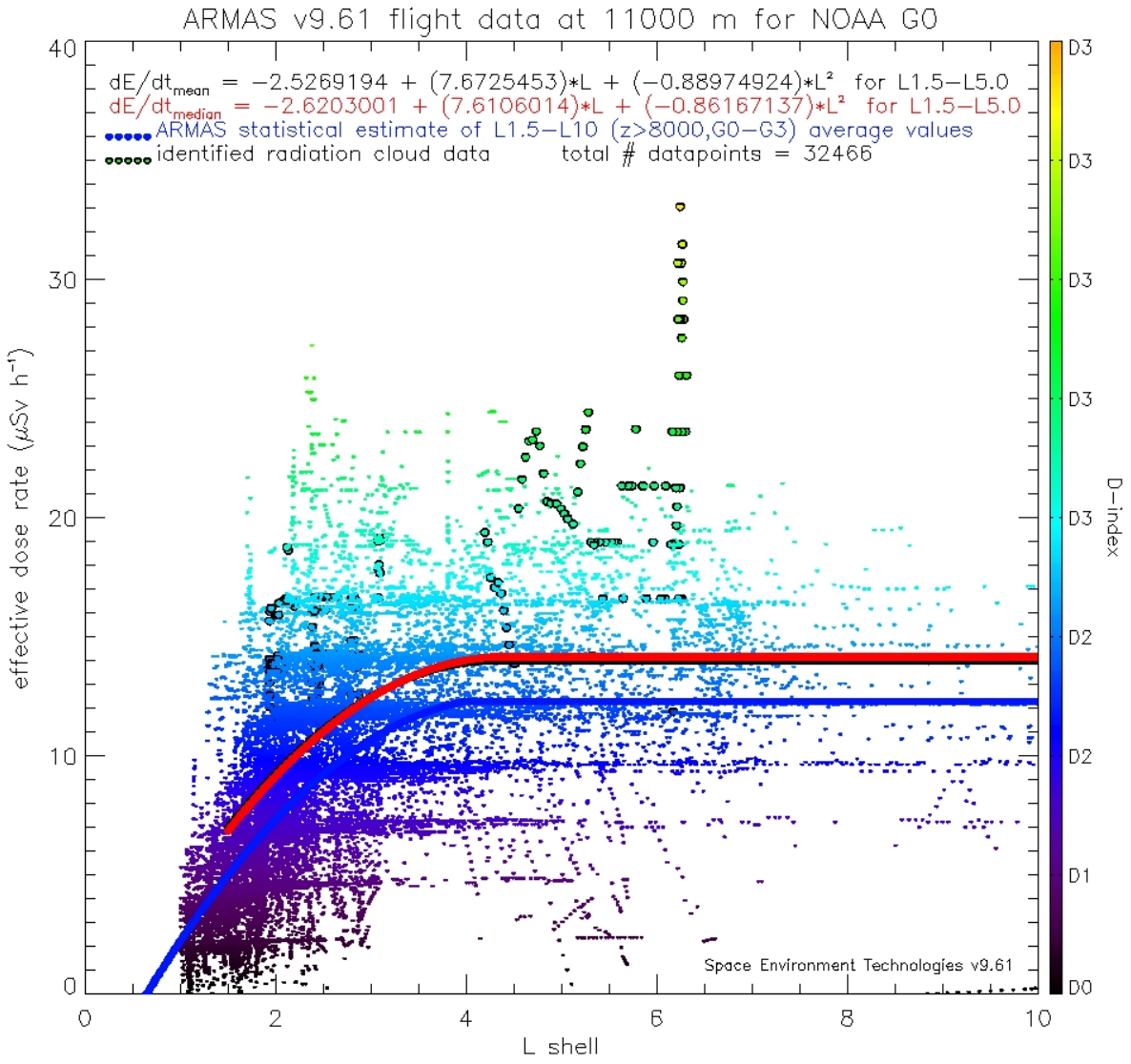

Fig. 4. ARMAS effective dose rates substantially increase between 4 ≤ L ≤ 5 above typical 11 km GCR values for quiet geomagnetic conditions during solar cycle 24 decline.

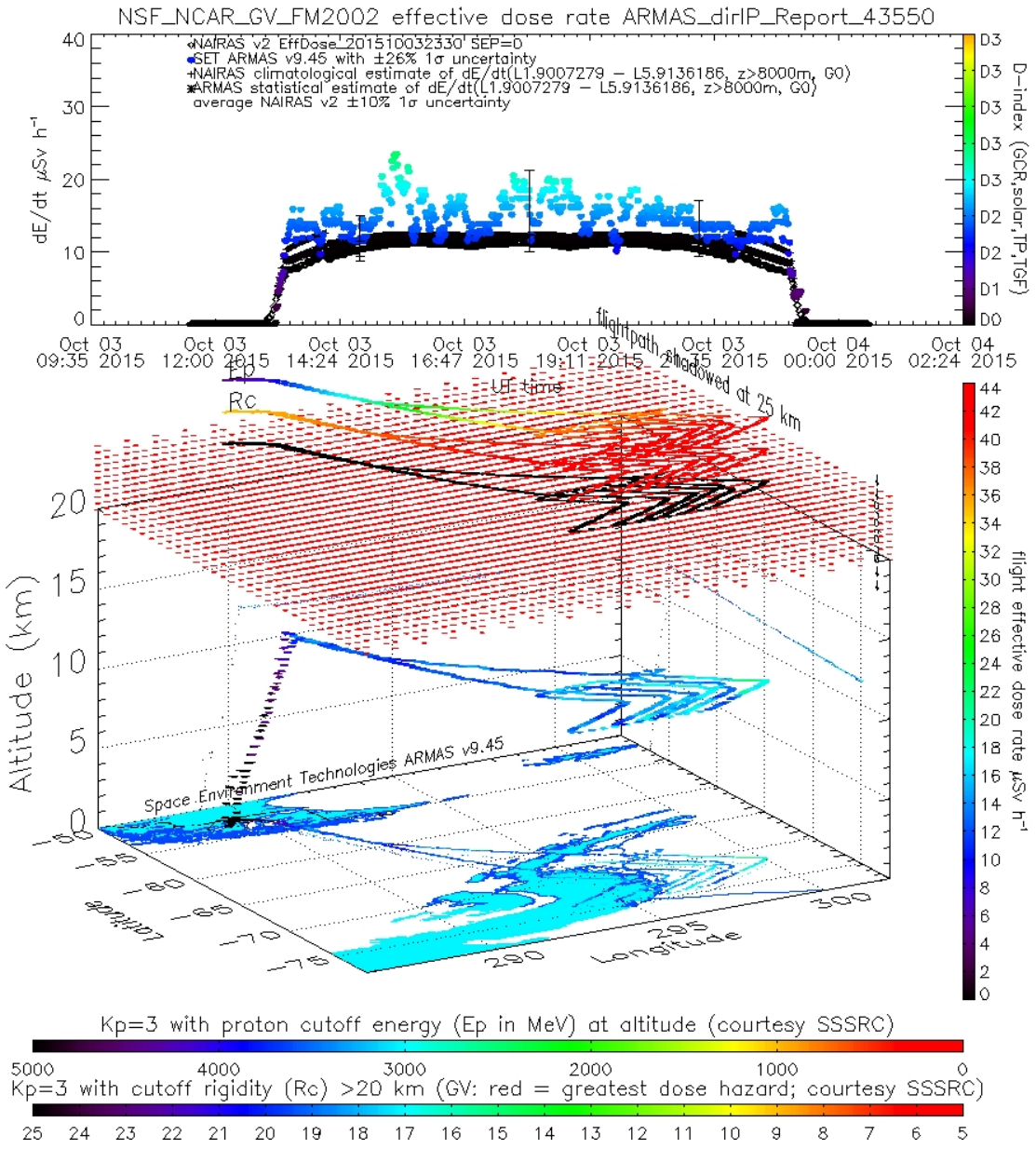

Fig. 5 The ARMAS 03 October 2015 G5 flight at 11.5 km and magnetic latitudes near –63° with doubled effective dose rate for ~1/2 hour; effective dose rate vs. time compared with NAIRAS (top panel black diamonds) and the flight geographical context with information related to proton cutoff energies and cutoff rigidities (bottom panel).

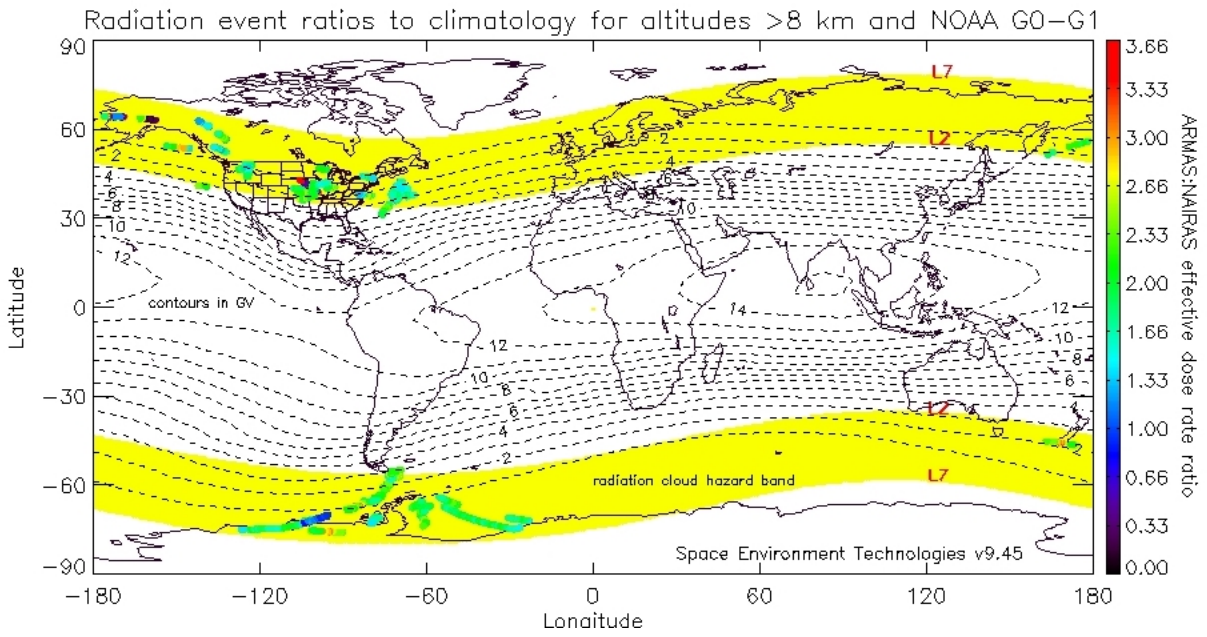

Fig. 6. One-minute ratios of ARMAS (measurements) to NAIRAS (model; GCR at this time) for all radiation events identified in Table 1, for all altitudes above 8 km, and for geomagnetic conditions of G0 and G1 on the NOAA G-scale. Cutoff rigidities are in units of GV (dashed lines) [Shea and Smart, 2012].

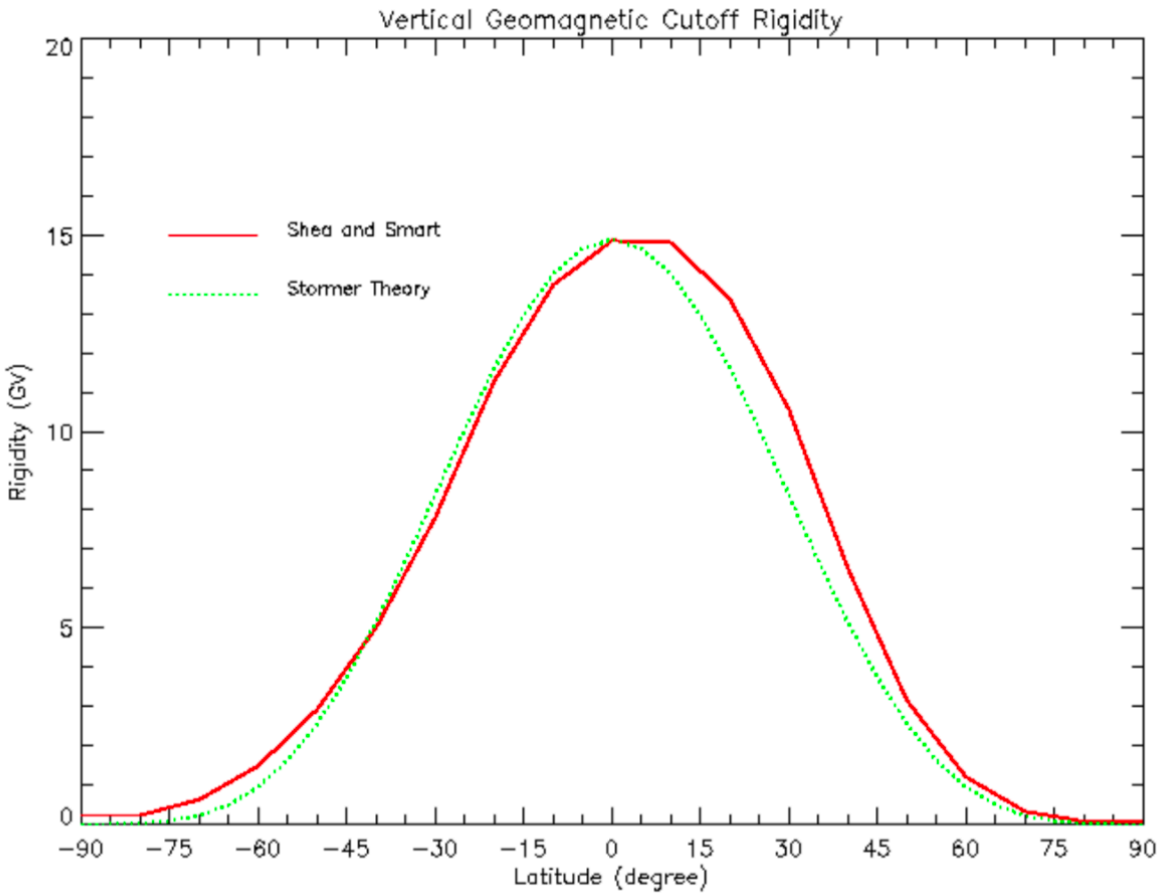

Fig. 7. Zonal-averaged vertical geomagnetic cutoff rigidity. The solid red line corresponds to the quiescent cutoff rigidities computed from particle trajectories and the IGRF model. The green dotted line is the analytical solution for the vertical cutoff rigidity using Störmer Theory.

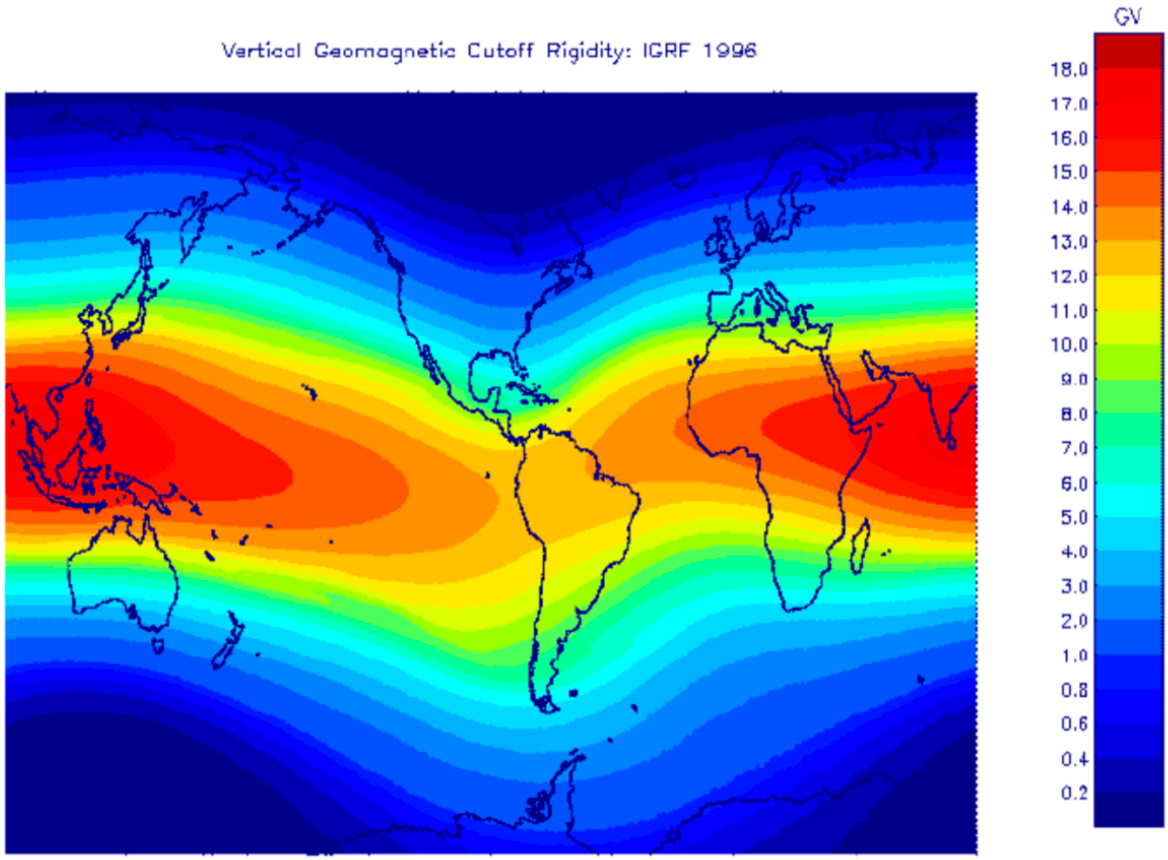

Fig. 8. Global grid of quiescent vertical geomagnetic cutoff rigidities (GV) calculated from charged particle trajectory simulations using the IGRF model for the 1996 epoch (solar cycle 23 minimum).

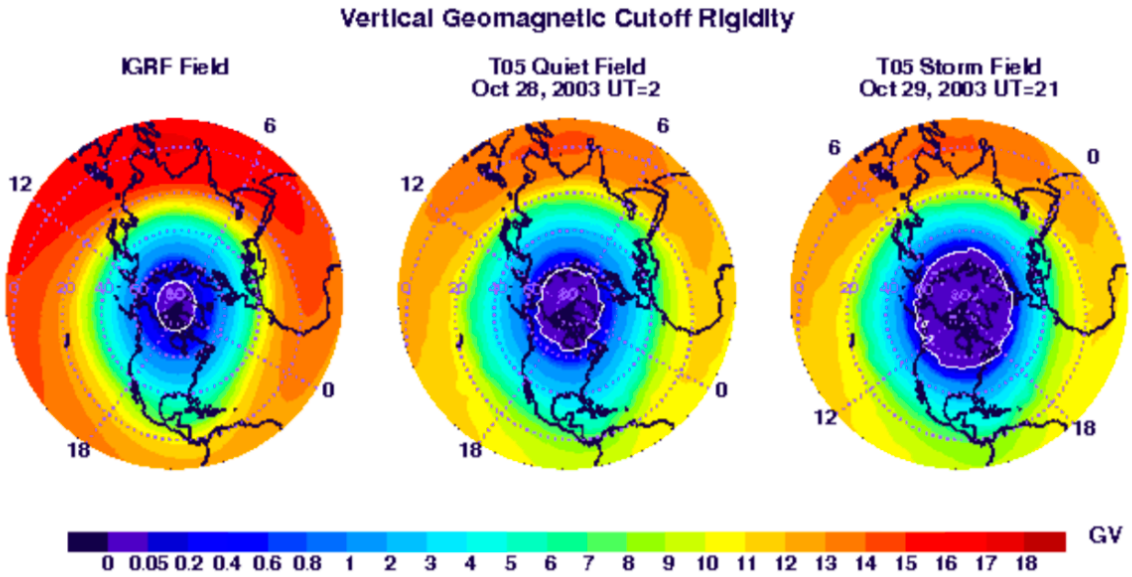

Fig. 9. Simulated vertical geomagnetic cutoff rigidity shown over the northern hemisphere in October 2003. The cutoff rigidities in the left column were calculated using the IGRF model. The cutoffs in the middle column were calculated using the TS05 model during a geomagnetically quiet period. Cutoff rigidities in the right column were calculated using the T05 model during the largest geomagnetically disturbed period of SEP event. Also shown are the magnetic latitude circles and the meridians at 0, 6, 12, and 18 magnetic local time.

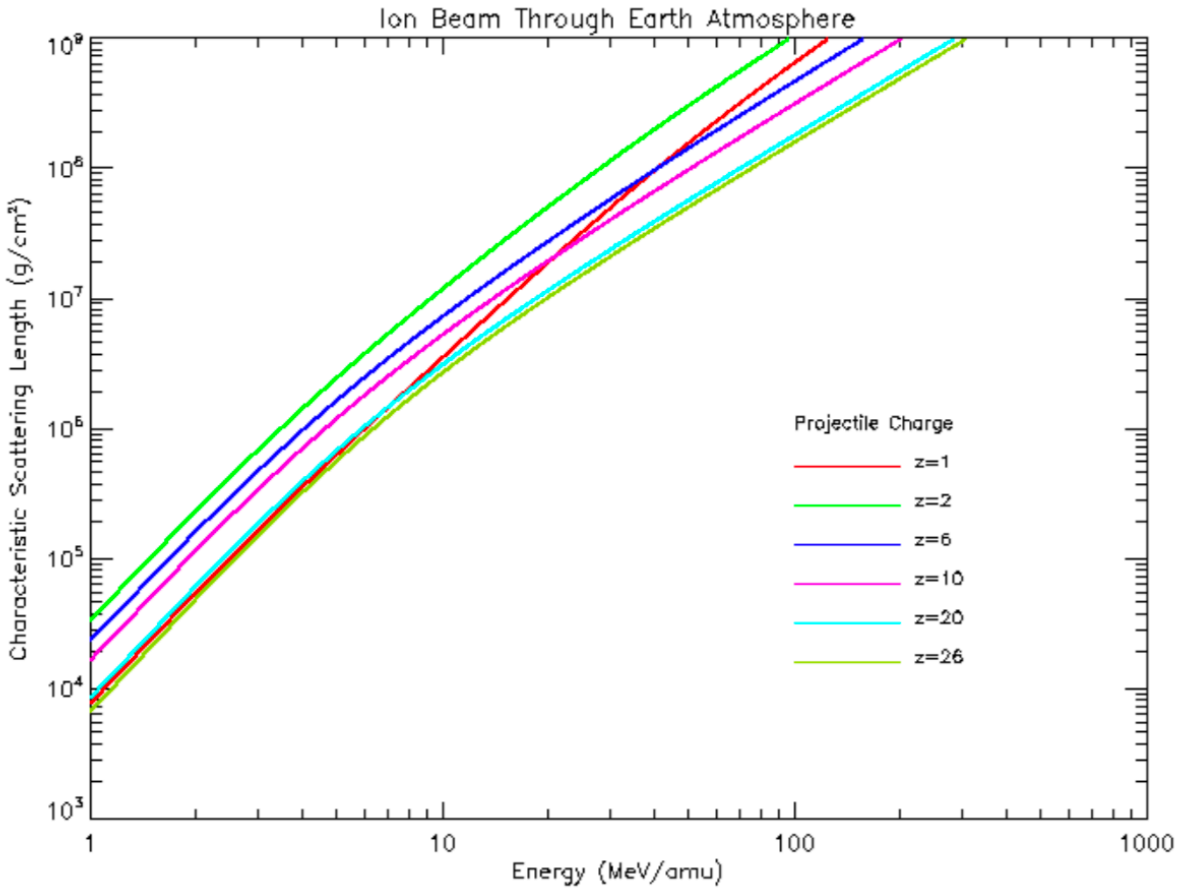

Fig. 10. Characteristic scattering length for ion beam transport through the Earth's atmosphere. The charge number (z) of the ion is specified in the legend.

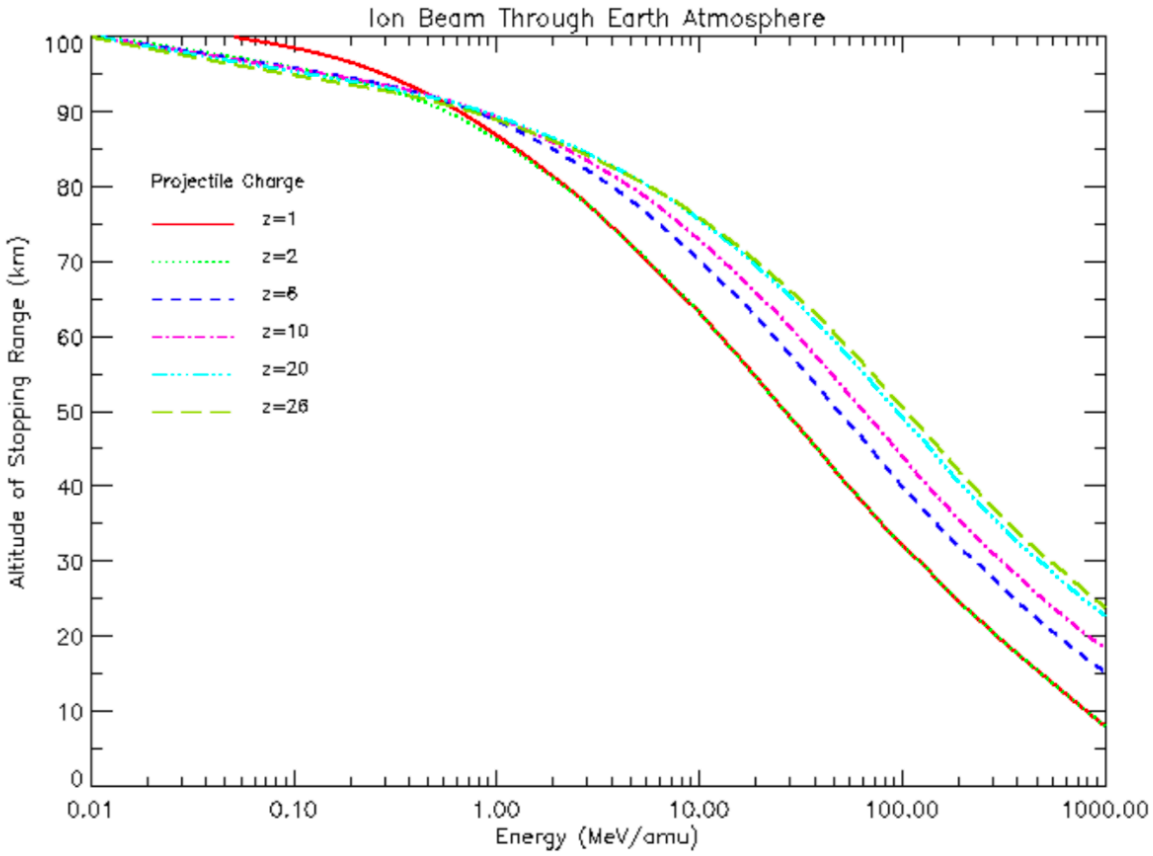

Fig. 11. Average range versus kinetic energy of an ion beam incident at the top of Earth's atmosphere. The charge number (z) of the ion is specified in the legend.

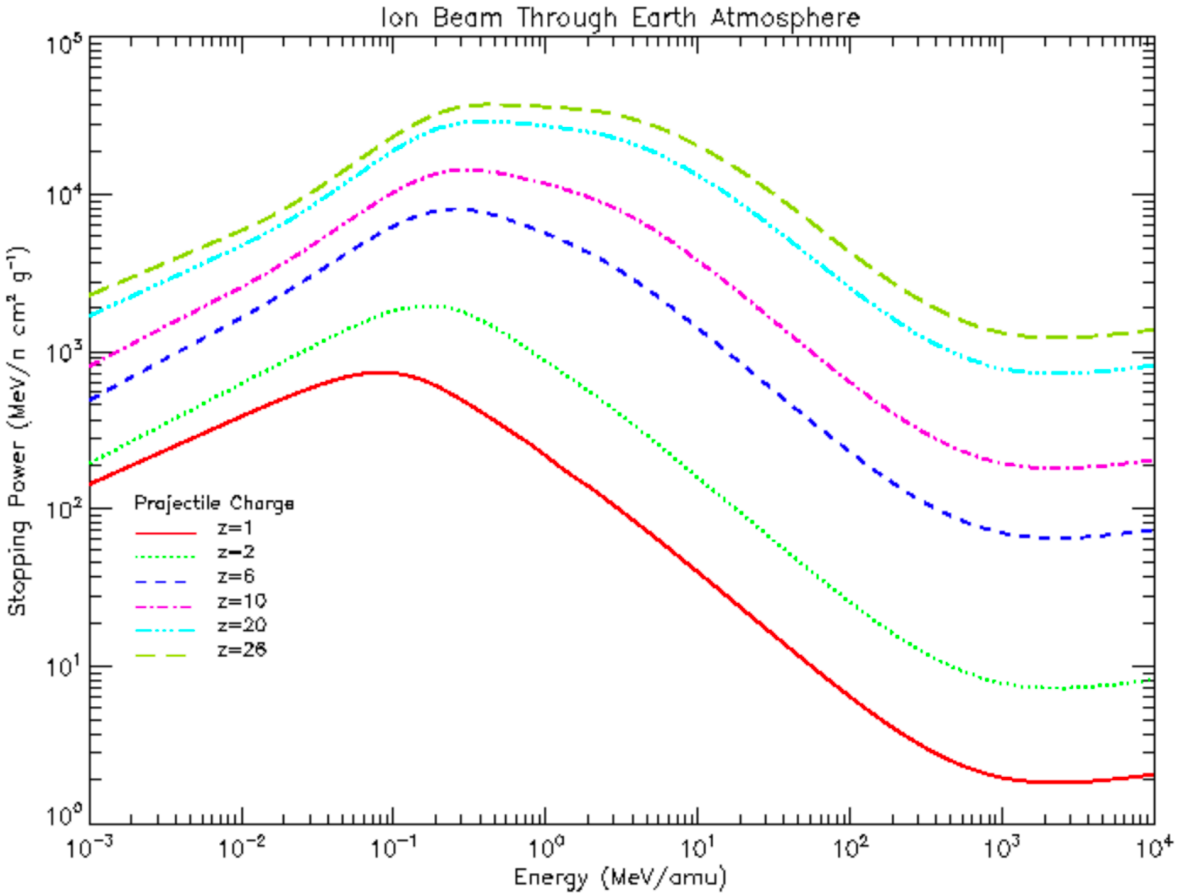

Fig. 12. Stopping power versus kinetic energy of incident ions on Earth's atmosphere. The charge number (z) of the ion is specified in the legend.

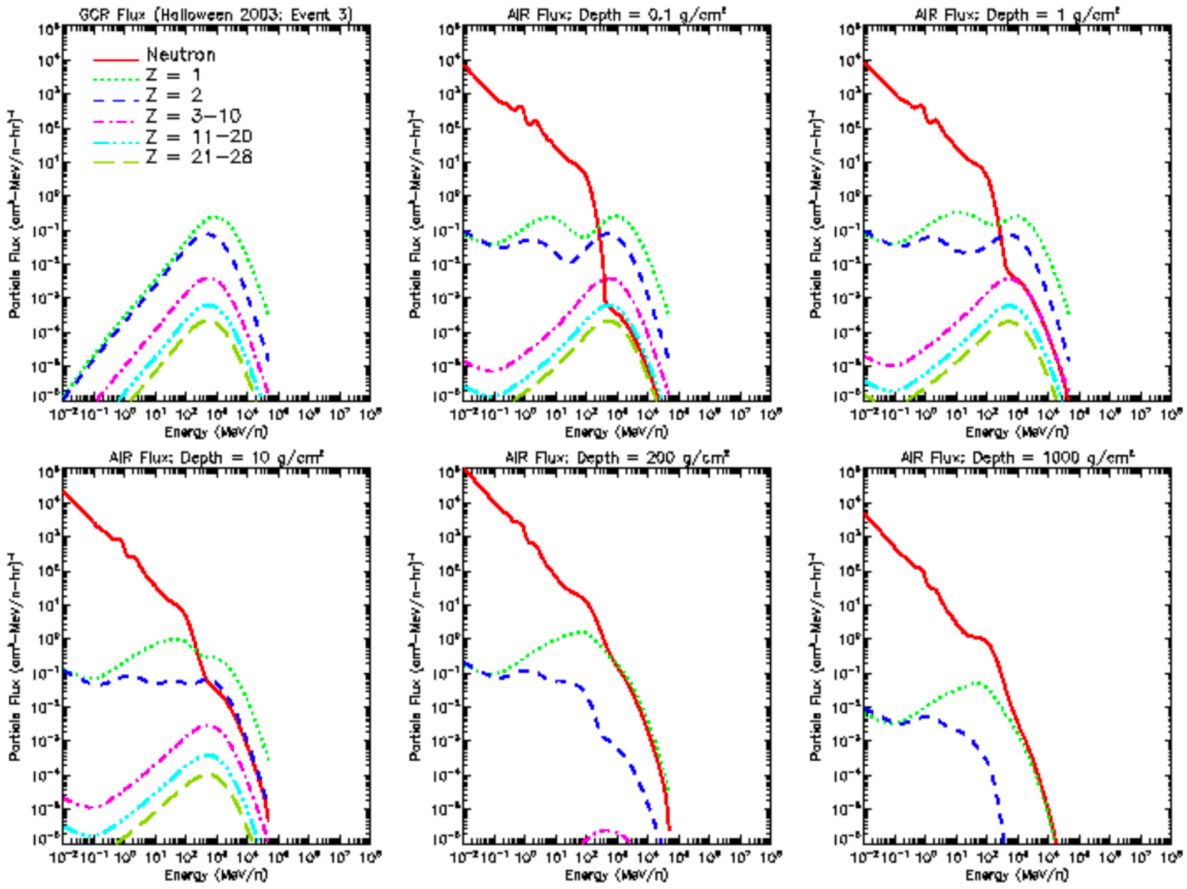

Fig. 13. Event-averaged GCR spectral fluence rates at zero vertical geomagnetic cutoff rigidity during the Halloween 2003 solar-geomagnetic storm [29 October 2003 (2100 UT) to 1 November (0000 UT)]. The panels show the fluence rates at different atmospheric depths. The typical cruising altitudes for commercial aircraft correspond to an atmospheric depth of roughly 200 g/cm^2. The fluence rates from different charge groups have been summed together to reduce the number of lines.

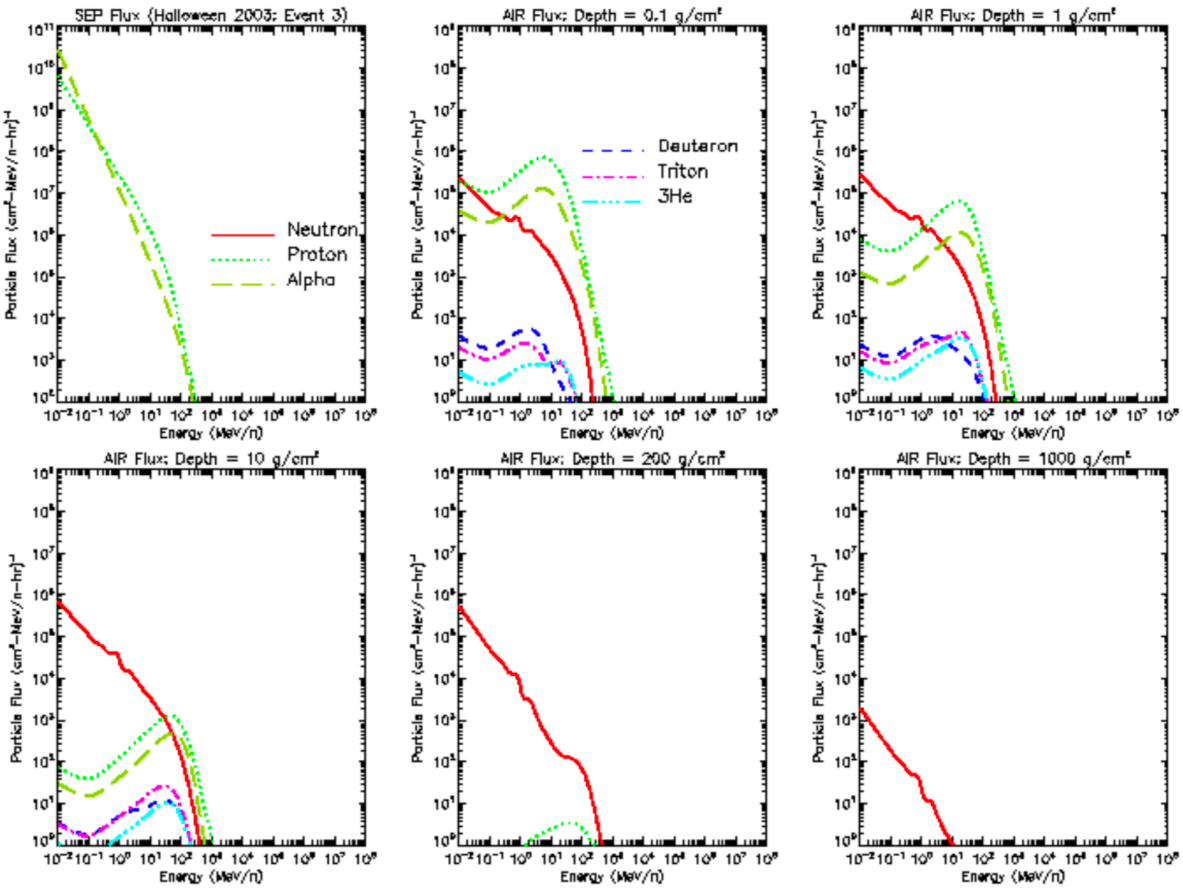

Fig. 14. Event-averaged SEP spectral fluence rates at zero vertical geomagnetic cutoff rigidity during the Halloween 2003 solar-geomagnetic storm [29 October 2003 (2100 UT) to 1 November (0000 UT)]. The panels show the fluence rates at different atmospheric depths. The typical cruising altitudes for commercial aircraft correspond to an atmospheric depth of roughly 200 g/cm^2.

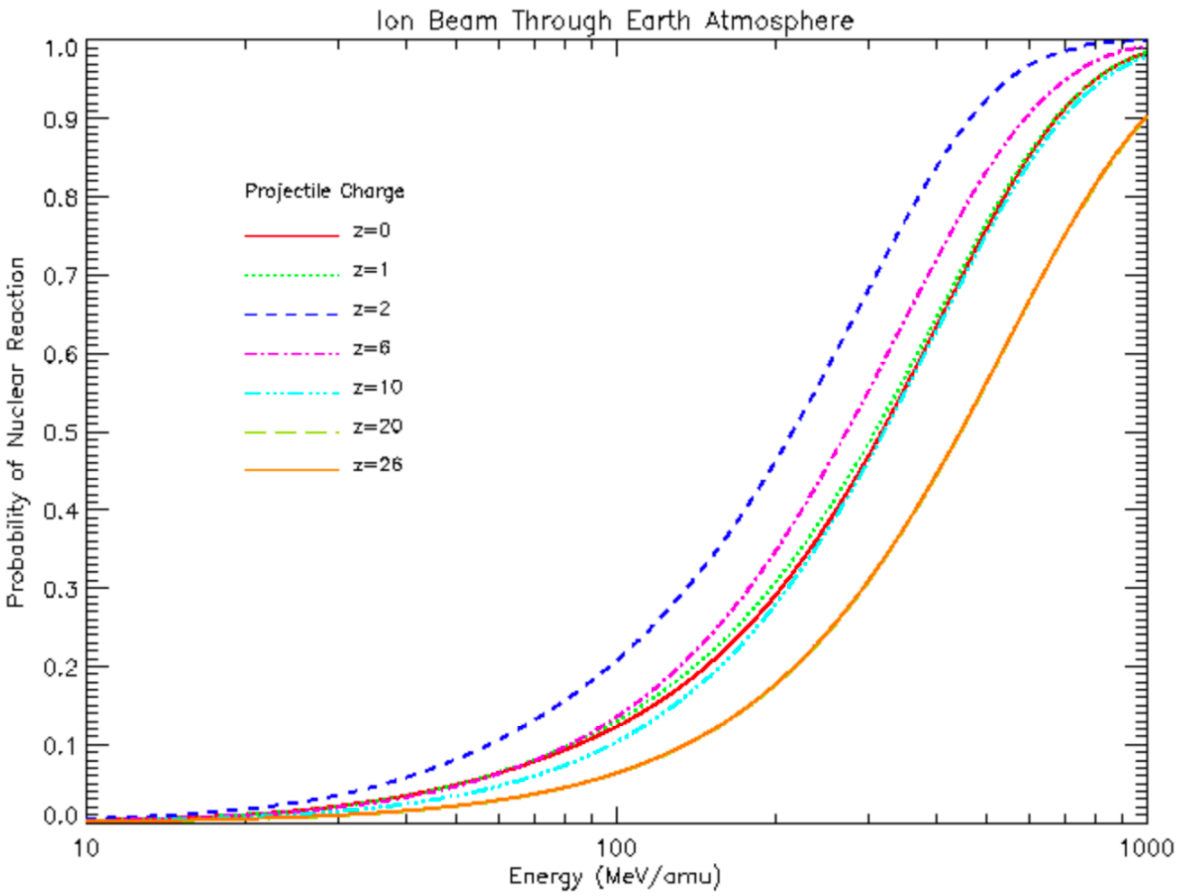

Fig. 15. Nuclear survival probability versus kinetic energy of an ion beam incident at the top of Earth's atmosphere. The charge number (z) of the ion is specified in the legend.

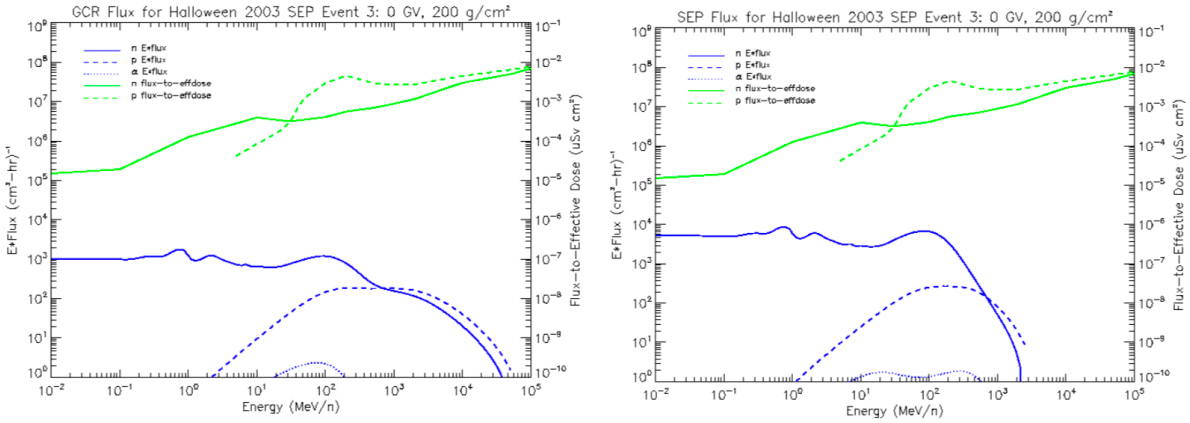

(a) GCR Component (b) SEP Component

Fig. 16. The green lines show the fluence-to-effective dose conversion coefficients. The blue lines show the product of the kinetic energy (MeV/amu) times the event-averaged spectral fluence rates for the Halloween 2003 storm period [29 October (2100 UT) to 1 November (0000 UT)]. The fluence rates were evaluated at zero vertical geomagnetic cutoff rigidity and at an atmospheric depth of 200 g/cm^2. The lines denote neutron quantities; dashed lines denote proton quantities; dotted lines denote alpha quantities. All quantities are shown for: (a) GCR component and (b) SEP component.

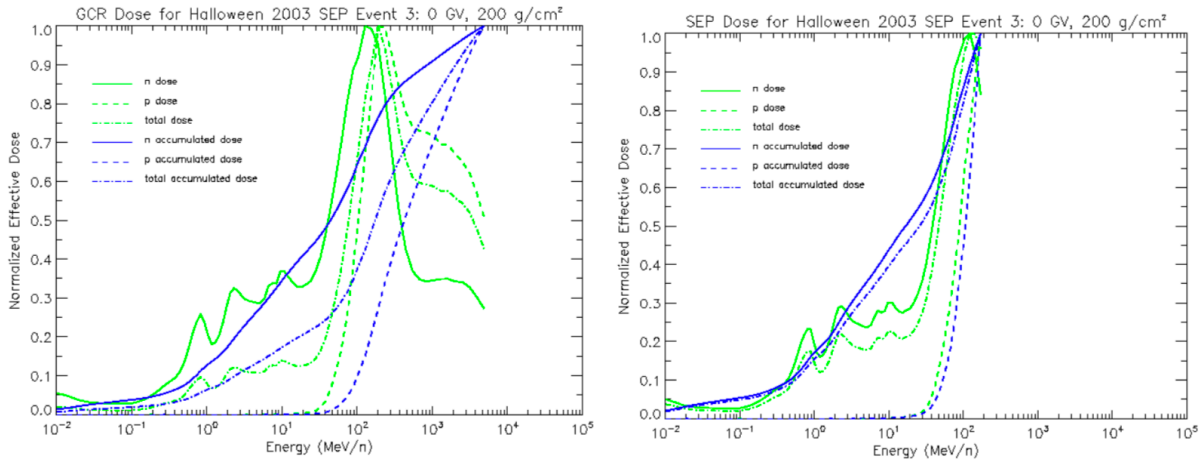

(a) GCR Component (b) SEP Component

Fig. 17. Normalized spectral effective dose rates evaluated during the Halloween 2003 storm period [29 October (2100 UT) to 1 November (0000 UT)] at zero vertical geomagnetic cutoff rigidity and at an atmospheric depth of 200 g/cm^2. The green lines show the spectral effective dose rate normalized to the peak in the spectrum. The blue lines are normalized to the spectrally integrated effective dose rate and show the accumulated effective dose rate as the spectral effective dose rate is integrated over energy. The solid lines denote neutron quantities; dashed lines denote proton quantities; dash-dot lines denote total quantities.